Responses to the comments of Referee #1

It is recommended that the manuscript be edited for English language use prior to publication. There are minor grammatical corrections needed throughout and occasional need for technical revision. One example is on p.6 line 164 where the authors state that "the NO measurements were basically reliable", which is not a sufficient description.

Reply: Thank you for the comments. We have made final corrections on grammar errors and some insufficient expressions throughout the main text. Please refer to the main text and supplementary information for detail.

Causes of a continuous summertime O_3 pollution event in Ji'nan, a central city in the North China Plain

Xiaopu Lyu[1], Nan Wang[2], Hai Guo[1*], Likun Xue[3], Fei Jiang[4], Yangzong Zeren[1], Hairong Cheng[5], Zhe Cai[4], Lihui Han[6], Ying Zhou[6]

[1] Air Quality Studies, Department of Civil and Environmental Engineering, The Hong Kong Polytechnic University, Hong Kong, China

[2] Division of Environmental Meteorology，Institute of Tropical and Marine Meteorology，China Meteorology Administration，Guangzhou，China

[3] Environment Research Institute, Shandong University, Ji'nan, China

[4] Jiangsu Provincial Key Laboratory of Geographic Information Science and Technology, International Institute for Earth System Science, Nanjing University, Nanjing, China

[5] Department of Environmental Engineering, School of Resource and Environmental Sciences, Wuhan University, Wuhan, China

[6] Department of Environmental Science, College of Environmental and Energy Engineering, Beijing University of Technology, Beijing, China

* Corresponding author: ceguohai@polyu.edu.hk

Abstract: In summer 2017, measurements of ozone (O_3) and its precursors were carried out at an urban site in Ji'nan, a central city in the North China Plain (NCP). A continuous O_3 pollution event was captured during August 4-11, with the maximum hourly O_3 reaching 154.1 ppbv. Model simulation indicated that local photochemical formation and regional transport contributed 14.0 ± 2.3 and 18.7 ± 4.0 ppbv/hr to the increase of O_3 during 09:00-15:00 local time (LT) in this event, respectively. For local O_3 formation, the calculated OH reactivities of volatile organic compounds (VOCs) and carbon monoxide (CO) were comparable between O_3 episodes and non-episodes ($p>0.05$), so was the OH reactivity of nitrogen oxides (NO_x). However, the ratio of OH reactivity of VOCs and CO to that of NO_x increased from 2.0 ± 0.4 s^{-1}/s^{-1} during non-episodes to 3.7 ± 0.7 s^{-1}/s^{-1} during O_3 episodes, which resulted in the change of O_3 formation mechanism from the VOC-limited regime before the O_3 pollution event to the transitional regime during the event. Correspondingly, the simulated local O_3 production rate during the event (maximum: 21.3 ppbv/hr) was markedly higher than that before the event ($p<0.05$) (maximum: 16.9 ppbv/hr). Given that gasoline and diesel exhaust made large contributions to the abundance of O_3 precursors and O_3 production rate, constraint on vehicular emissions is the most effective strategy to control O_3 pollution in Ji'nan. The NCP has been confirmed as a source region of tropospheric O_3, where the shift of regimes controlling O_3 formation like the case presented in this study can be expected across the entire region, due to the substantial reductions of NO_x emissions in recent years.

Keywords: Ozone, local formation, regional transport, volatile organic compound, North China Plain

1 Introduction

Air pollution in the North China Plain (NCP), the largest alluvial plain of China consisting of Beijing, Tianjin and many cities in Hebei, Shandong, and Henan provinces, has attracted much attention in recent years. While the annual average concentration of $PM_{2.5}$ (particulate matters with aerodynamic diameter less than or equal to 2.5 μm) has been reduced under concerted efforts on emission restrictions (Zhang et al., 2015; Lang et al., 2017), the tropospheric ozone (O_3) pollution, which is less visible than haze but may be equivalently harmful to human health, is still severe. At a regional receptor site of the NCP in a mountainous area to the north of Beijing, Wang et al. (2006) reported the maximum hourly O_3 of 286 ppbv. A year-round observation of O_3 at 10 urban sites in Beijing indicated frequent O_3 non-attainments (hourly O_3 > 100 ppbv) through May to August of 2013 (Wang et al., 2015a). Hourly O_3 mixing ratio of up to 120 ppbv was reported on Mt. Tai, the highest mountain in the NCP (1534 m a.s.l.) (Gao et al., 2005). All these studies revealed the significant photochemical O_3 pollution over the entire NCP. Moreover, O_3 has been increasing in the NCP during the last decades (Zhang et al., 2014; Zhang et al., 2015). The increase rate of O_3 at an urban site in Beijing from 2005 to 2011 was quantified as 2.6 ppbv/year (Zhang et al., 2014), comparable to that (1.7-2.1 ppbv/year) at Mt. Tai in the summer between 2003 and 2015 (Sun et al., 2016). Overall, the NCP suffers from severe O_3 pollution, which is even aggravating.

Apart from the intrusion of stratospheric O_3 in some places with high elevations (Cooper et al., 2005; Lin et al., 2015), photochemical formation is the main source of the ground-level O_3. Volatile organic compounds (VOCs), carbon monoxide (CO) and nitrogen oxides (NO_x) are key precursors of tropospheric O_3 (Crutzen, 1973; Chameides and Walker, 1973; Carter, 1994; Carter et al., 1995). The general chemical reactions R(1) - R(5) show the production of O_3 from the OH initiated oxidation of hydrocarbons (RH) (Jenkin et al., 1997; Atkinson, 2000; Jenkin and Clemitshaw, 2000).

$$RH + OH + O_2 \rightarrow RO_2 + H_2O \qquad (R1)$$

$$RO_2 + NO \rightarrow RO + NO_2 \qquad (R2)$$

$$RO + O_2 \rightarrow \text{Carbonyls} + HO_2 \qquad (R3)$$

$$HO_2 + NO \rightarrow OH + NO_2 \qquad (R4)$$

$$NO_2 + O_2 + hv \rightarrow O_3 + NO \qquad (R5)$$

The production of O_3 is generally limited by VOCs or NO_x or co-limited by both VOCs and NO_x, depending upon the chemical compositions of the air, particularly the ratio between OH reactivity of VOCs and NO_x (OH reactivity is the sum of the products of O_3 precursors concentrations and the reaction rate constants between O_3 precursors and OH). Xue et al. (2014) indicated that the formation of O_3 was limited by NO_x in Lanzhou in summer, consistent with the findings of Liu et al. (2010) who proved that NO_x-limited regime dominated O_3 formation in most areas of northwestern China. In southwestern China, O_3 formation was diagnosed as VOC-limited in Chengdu, but NO_x-limited in Pengzhou due to the large amount of emissions from petrochemical industry (Tan et al., 2018a). Lyu et al. (2016) reported the VOC-limited regime in Wuhan, central China. The VOC-limited regime has also been repeatedly confirmed for O_3 formation in Shanghai (Xue et al., 2014; Xing et al., 2017) and Nanjing (Ding et al., 2013), eastern China. In the Pearl River Delta of southern China, it was found that O_3 formation was generally limited by VOCs in the southwest, while limited by NO_x in the northeast (Ye et al., 2016). In the NCP, both Han et al. (2018) and Xing et al. (2018) summarized that VOCs limited the production of O_3 in most urban areas. However, in the suburban and rural areas, O_3 formation was generally in the transitional regime, *e.g.* Yucheng (Zong et al., 2018), or limited by NO_x, *e.g.* Wangdu (Tan et al., 2018b). From a historical perspective, Jin et al. (2017) pointed out that the sensitivity of O_3 formation to VOCs increased in most Chinese cities, however decreased in some megacities (such as Beijing and Shanghai) due to the stringent control of NO_x emissions in recent years. Different VOCs play non-equivalent roles in O_3 formation. Alkenes, aromatics and carbonyls can be readily oxidized by oxidative radicals (*e.g.* OH) or photolyzed (applicable for carbonyls), leading to O_3 formation (Cheng et al., 2010; Guo et al., 2013). Therefore, the sources with large quantities of emissions of these VOCs generally make considerable contributions to the photochemical production of ground-level O_3. For example, Cheng et al. (2010) pointed out that carbonyls increased the peak O_3 production rates at a rural site and at a suburban site in South China by 64% and 47%, respectively. Solvent based industry and paint solvent usage with intensive emissions of aromatics were responsible for more than half of O_3 formation potential in Shanghai (Cai et al., 2010). Carbonyls and alkenes accounted for 71-85% of the total OH reactivity of VOCs in Beijing (Shao et al., 2009).

In addition to the chemical processes, meteorological conditions also play significant roles in the formation, transport and accumulation of O_3. Studies (Chan and Chan, 2000; Huang et al., 2005) indicated that tropical cyclone (typhoon as the mature form) and continental anticyclone are the most common synoptic systems conducive to O_3 pollution in coastal cities of South China. Many O_3 episodes in East China occurred under the control of the west Pacific subtropical high pressure (He et al., 2012; Shu et al., 2016). In the NCP (North China), the summertime O_3 pollution is generally accompanied with weak high pressure systems (Wang et al., 2010). Furthermore, O_3 pollution is also related to the topography. For example, the mountains to the north and west of Beijing lead to upslope winds (valley breeze) in daytime, which transport the polluted air masses laden with O_3 and/or O_3 precursors from the NCP to Beijing (Lin et al., 2008). Overall, the causes of O_3 pollution are complicated and need to be analyzed case by case.

The NCP is the region with the largest emissions of many air pollutants, such as VOCs and NO_x, in China (Gu et al., 2014; Li et al., 2017), partially accounting for the severe O_3 pollution there. In addition, O_3 pollution in the NCP is closely related to the synoptic systems and topographic features (Chen et al., 2009; Zhang et al., 2016). For example, the strong photochemical production of O_3 in urban plumes of Beijing was found by Wang et al. (2006), while the contribution of regional transport was revealed by the enhanced O_3 production at a rural site in the NCP under southerly winds (Lin et al., 2008). Through the review of synoptic systems in the NCP from 1980 to 2013, Zhang et al. (2016) concluded that the air quality was generally unhealthy under weak East Asian Monsoons. Moreover, a decadal statistical analysis indicated that meteorological factors explained ~50% of the O_3 variations in Beijing (Zhang et al., 2015). Despite many previous studies, the evolutions of the synoptic and photochemical processes in O_3 pollution events and their contributions to the non-attainment of O_3 have been seldom looked into in the NCP. Besides, the local and regional contributions to the elevated O_3 in the NCP are not unambiguously quantified, limited by the deficiencies in model representation of either physical or local chemical processes. The situation was even much worse for Ji'nan, the capital of Shandong province. As early as 2000s, studies (Shan et al., 2008; Yin et al., 2009) reported the maximum hourly O_3 of 143.8 ppbv and 147.8 ppbv in June 2004 and 2005, respectively. Even higher O_3 (198 ppbv) was observed at a rural site downwind of Ji'nan in June 2013 (Zong et al., 2018). However, almost no study was carried out to explore the mechanisms responsible for high O_3 there, though it has been confirmed that air pollution in the cities like Ji'nan in the NCP influenced air quality in Beijing (Lin et al., 2008; Wang et al., 2010). To better understand O_3 pollution in the NCP, this study investigated the causes of an O_3 episode event lasting for eight days in Ji'nan in summer 2017. The analyses presented here focused on the synoptic systems dominating Shandong Peninsula during this event; the chemical profiles of O_3 and O_3 precursors; and the simulation of factors contributing to O_3 in Ji'nan with the aid of a chemical transport model and a photochemical box model. In addition, we proposed feasible O_3 control measures based on the source-resolved OH reactivity of VOCs and NO_x.

2 Methodology

2.1 Site description

The air quality monitoring and sample collection were carried out on the rooftop of a 7-story building on the campus of Shandong University from July 15 to August 14, 2017. The campus is located in the urban area of Ji'nan, and the site is about 50 m from a main road (Shanda South Road) outside the campus. Figure 1 shows the locations of the sampling site (36.68 °N, 117.07 °E, 22 m a.g.l.) and the surrounding air quality monitoring stations (AQMSs) set up by China National Environmental Monitoring Center (CNEMC). Also shown are the observed O_3 and rainfall averaged over August 4-11, 2017 when the O_3 episode event occurred in Ji'nan. It is noteworthy that the days with maximum hourly O_3 exceeding 100 ppbv (Grade II of National Ambient Air Quality Standard) were defined as O_3 episode days. The hourly O_3 values at the

AQMSs were obtained from the website of CNEMC (http://www.cnemc.cn/). The high O_3 levels at almost all the AQMSs in the NCP (Figure 1 (a)) indicated a regional O_3 pollution event in this period. In view of the comparable O_3 mixing ratios observed at our sampling site to those at the surrounding AQMSs, we believe that the observations at our sampling site to some extent represented the characteristics of this regional pollution event. This was confirmed by the strong influences of regional transport on O_3 variations at the site, as discussed in section 3.3.

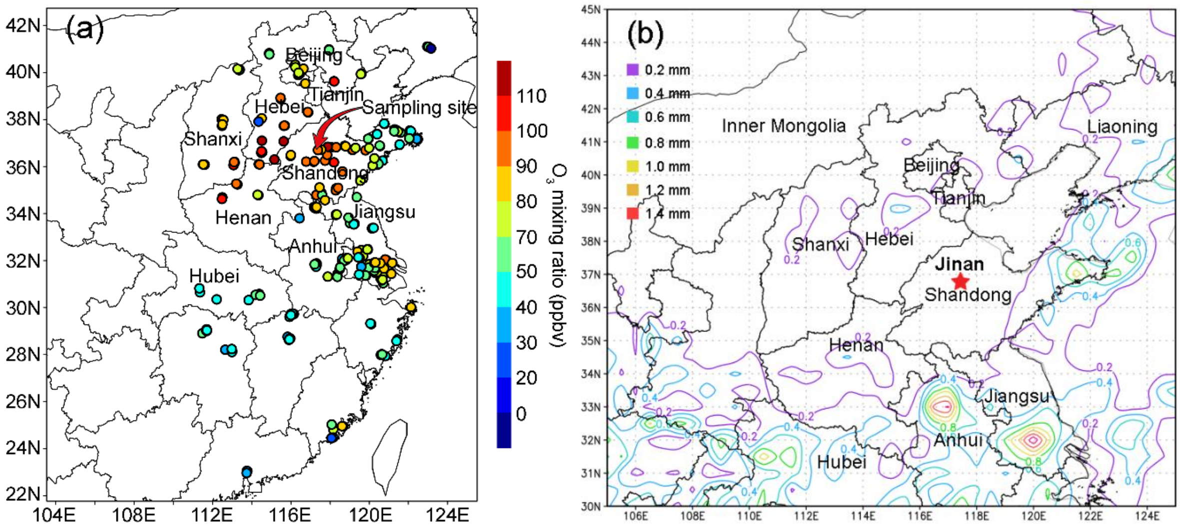

Figure 1 (a) Locations of the sampling site and the CNEMC AQMSs, and the average observed O_3 at 14:00 LT on August 4-11, 2017 (colored circles). The sampling site is overlapped with the nearest AQMS in Ji'nan. (b) Rainfall distribution, in millimeters (mm), averaged over August 4-11, 2017.

2.2 Air quality monitoring and sample collection

2.2.1 Continuous monitoring of air pollutants and meteorological parameters

O_3, NO and NO_2 were continuously monitored at the sampling site between July 15 and August 14, 2017. The air was drawn through a 4 m Teflon tube by the built-in pumps of the trace gas analyzers at the total flow rate of 2 L/min (1.4 L/min for O_3 analyzer and 0.6 L/min for NO_x analyzer). The inlet was located ~1 m above the rooftop of the building. O_3 and NO/NO_x were detected with a UV photometric based analyzer and a chemiluminescence NO-NO_2-NO_x analyzer, respectively (see Table S1 for the specifications). The lowest NO observed during the sampling period was 2.4 ppbv, 6 times the detection limit (DL) of the NO_x analyzer (0.4 ppbv).

Since the measurement accuracy of the analyzer was <15%, the DL was low enough to not influence the accurate measurements of NO in this study. NO_2 was calculated from the difference between NO and NO_x. Studies indicated that NO_2 monitored with chemiluminescence was generally overestimated due to the conversion of the total odd nitrogen (NO_y) to NO by molybdenum oxide catalysts (McClenny et al., 2002; Dunlea et al., 2007; Xu et al., 2013). The positive bias was more significant in more aged air masses, resulting from higher levels of NO_z (NO_z = NO_y - NO_x) (Dunlea et al., 2007). The average overestimation of NO_2 was 22% in Mexico City, which even increased to 50% in the afternoon (Dunlea et al., 2007). Xu et al. (2013) suggested that the chemiluminescence monitors overestimated NO_2 by less than 10% in urban areas with fresh emission of NO_x, but the positive bias went up to 30-50% at the suburban sites. As described in section 2.1, our sampling site was located in the urban area of Ji'nan and was only ~50 m to a main road. Therefore, we infer that NO_2 might not be significantly overestimated in this study. However, larger overestimation could be expected during O_3 episodes, when the stronger photochemical reactions caused higher production of NO_z. According to Xu et al. (2013), we adopted 30% (minimum bias in suburban area) and 10% (maximum bias in urban area) as the maximum fraction of NO_2 overestimation during episodes and non-episodes at this urban site, respectively. The influences of the NO_2 measurement interferences on the results were discussed where necessary.

The hourly concentrations of sulfur dioxide (SO_2) and CO were acquired from a nearest AQMS, which is ~1 km from our sampling site. Year-round monitoring of inorganic trace gases was conducted at this AQMS. The air was drawn into the analyzers at a flow of 3 L/min through an inlet, ~1 m above the rooftop of a 5-story building (~ 16 m a.g.l.). The specifications of the analyzers deployed at the AQMS are also provided in Table S1. The hourly concentrations of O_3 and NO_2 measured at the AQMS (NO data was not available at the CNEMC website) agreed well with those observed at our sampling site, with the slope of 1.04 (R^2 = 0.82) and 1.13 (R^2 = 0.71) for O_3 and NO_2 in the linear least square regressions, respectively (Figure S1). Due to the differences in analyzers and/or in sources and sinks of air pollutants between the two sites, the agreements were worse at low mixing ratios for both O_3 and NO_2. Therefore, we only used SO_2 and CO monitored at the AQMS in this study, which had lower photochemical reactivity than O_3 and NO_2, and were more homogeneous at a larger scale.

In addition, the meteorological parameters, including wind speed, wind direction, pressure, temperature and relative humidity, were monitored at the sampling site by a widely used weather station (China Huayun group, Model CAWS600-B). The daily total solar radiation was obtained from the observations at a meteorological station in Ji'nan (36.6 °N, 117.05 °E, 170.3 m a.s.l), 9 km to our sampling site.

2.2.2 Sample collection and chemical analysis

The VOC and oxygenated VOC (OVOC) samples were collected on 9 selective days (*i.e.*, July 20 and 30, August 1, 4-7 and 10-11), referred to as VOC sampling days hereafter. The days were selected to cover the periods with relatively high and normal levels of O_3. The high O_3 days were forecasted prior to sampling based on the numerical simulations of meteorological conditions and air quality. In total, 6 out of 9 VOC sampling days were O_3 episode days with the maximum hourly O_3 values ranging from 100.4 to 154.1 ppbv. On each day (regardless of episode or non-episode), 6 VOC/OVOC samples were collected between 08:00 and 18:00 LT every 2 hours with the duration of 1 hour for VOC and 2 hours for OVOC samples. VOC samples were collected with 2 L stainless steel canisters which were cleaned and evacuated before sampling. A flow restrictor was connected to the inlet of the canister to guarantee 1 hour sampling. OVOC were sampled with the 2,4-dinitrophenylhydrazine (DNPH) cartridge, in front of which an O_3 scrubber was interfaced to remove O_3 in the air. A pump was used to draw the air through the DNPH cartridge at a flow of 500 mL/min. After sampling, all the DNPH cartridges were stored in a refrigerator at 4 °C till chemical analysis.

VOC samples were analyzed with a gas chromatograph-mass selective detector/flame ion detector/electron capture detector system (Colman et al., 2001). In total, 85 VOCs, including 59 hydrocarbons, 19 halocarbons and 7 alkyl nitrates, were quantified. The overall ranges of the DL, accuracy and precision for VOCs analysis were 1-154 pptv, 1.2-19.8% and 0.1-17.9%, respectively. The analysis results given by this system have been compared with those analyzed by UCI and good agreements were achieved (Figure S2). OVOC samples were eluted with 5 mL acetonitrile, followed by analysis with the high performance liquid chromatography. The DL, accuracy and precision for the detected OVOCs species were within the range of 3-11 pptv, 0.32-0.98% and 0.01-1.03%, respectively.

2.3 Model configuration

2.3.1 Chemical transport model

To analyze the processes contributing to high O_3 in Ji'nan, a chemical transport model, i.e. the Weather Research Forecast-Community Multi-scale Air Quality (WRF-CMAQ), was utilized to simulate O_3 in this study. WRF v3.6.1 was run to provide the offline meteorological field for CMAQ v5.0.2. A two-nested domain was adopted with the resolution of 36 km (outer domain) and 12 km (inner domain), respectively. As shown in Figure S3, the outer domain covered the entire continental area of China aiming to provide sufficient boundary conditions for the inner domain, which specifically focused on eastern China.

We used the 2012-based Multi-resolution Emission Inventory for China (MEIC) to provide anthropogenic emissions of air pollutants, which was developed by Tsinghua University specific for China, with the grid resolution of 0.25°×0.25° (Zhang et al., 2007; He, 2012). Five emission sectors, namely transportation, agriculture, power plant, industry and residence were included in MEIC. The emission inventory was linearly interpolated to the domains with consideration of the earth curvature effect. For grids outside China, the air pollutant emissions were derived from INTEX-B (Intercontinental Chemical Transport Experiment-Phase B) Asian emission inventory (Zhang et al., 2009). Consistent with many previous studies (Jiang et al., 2010; Wang et al., 2015b), the Model of Emissions of Gases and Aerosols from Nature (MEGAN) was used to calculate the biogenic emissions. The physical and chemical parameterizations for WRF-CMAQ were generally identical to those described in Wang et al. (2015b), with the following improvements. Firstly, the carbon bond v5 with updated toluene chemistry (CB05-TU) was chosen as the gas phase chemical mechanism (Whitten et al., 2010). Secondly, a single-layer urban canopy model (Kusaka and Kimura, 2004) was used to model the urban surface-atmosphere interactions. Thirdly, the default 1990s U.S. Geological Survey data in WRF was replaced by adopting the 2012-based moderate resolution imaging spectroradiometer (MODIS) land cover data for eastern China. The substitution was performed to update the simulation of boundary meteorological conditions (Wang et al., 2007).

An integrated process rate (IPR) module incorporated in CMAQ was used to analyze the processes influencing the variations of O_3. Through solving the mass continuity equation established between the overall change of O_3 concentration across time and the change of O_3 concentration caused by individual processes, including horizontal diffusion (HDIF), horizontal advection (HADV), vertical diffusion (VDIF), vertical advection (VADV), dry deposition (DDEP), net effect of chemistry (CHEM) and cloud processes (CLD), the O_3 variation rates induced by individual processes were determined. Note that since the estimate of CHEM is influenced by the estimate of O_3 precursor emissions, the simulation of meteorological conditions and the chemical mechanism, all the three aspects should be taken into account wherever CHEM is discussed. The IPR analysis has been widely applied in diagnosis of processes influencing O_3 pollution (Huang et al., 2005; Wang et al., 2015b). Since the field observations were conducted near the surface (~ 22 m a.g.l.), and the box model (section 2.3.2) was constrained by the observations, the modeling results on the ground-level layer were extracted from WRF-CMAQ for analyses in this study.

2.3.2 Photochemical box model

We also utilized a Photochemical Box Model incorporating the Master Chemical Mechanism (PBM-MCM) to study the in situ O_3 chemistry, thanks to the detailed (species-based) descriptions of VOC degradations in the MCM (Saunders et al., 2003; Lam et al., 2013). The PBM model was localized to be applicable in Ji'nan, with the settings of geographic coordinates, sunlight duration and photolysis rates. The photolysis rates were calculated by the TUV model (Madronich and Floke, 1997). Specifically, the geographical coordinates, date and time were input into the TUV model to initialize the calculation of solar radiation with the default aerosol optical depth (AOD), cloud optical depth (COD), surface albedo and other parameters. Then, COD was adjusted to make the calculated daily total solar radiation progressively approach the observed value. When the difference between the calculated and observed solar radiation was less than 1%, the input parameters with the adjusted COD were accepted. Based on the settings, the hourly solar radiations and the photolysis rates of O_3 ($J(O^1D)$) and NO_2 (JNO_2) were calculated by the TUV model, and applied to the PBM-MCM for O_3 chemistry modelling. Table S2 shows the daily maximum $J(O^1D)$ and JNO_2 on the VOC sampling days. The MCM v3.2 (http://mcm.leeds.ac.uk/MCM/) consists of 17,242 reactions among 5,836 species. The mixing ratios of O_3 and its precursors at 00:00 on each day were used as the initial conditions for each day's modelling. The initial O_3 therefore represented O_3 left over from the days before the modelling day, and partially accounted for the primary OH production. Hourly concentrations of 46 VOCs, 4 OVOCs and 4 trace gases (SO_2, CO, NO and NO_2), as well as hourly meteorological parameters (temperature and relative humidity) were taken as inputs to constrain the model. O_3, as the species to be modeled, was not input except for the setting of initial conditions. The Freon, cycloalkanes and methyl cycloalkanes with low O_3 formation potentials were not included in model inputs either. Also excluded were the species whose concentrations were lower than the DLs in more than 20% samples, such as the methyl hexane and methyl heptane isomers. For the hours when measurement data were not available, the concentrations were obtained with linear interpolation. Some secondary species, such as formaldehyde (HCHO), acetaldehyde and acetone, were input into the model to constrain the simulation. Since other secondary species, *e.g.*, PAN and HNO_3 were not observed in this study, their concentrations were calculated by the model. The model simulated dry depositions of all the chemicals, and the deposition velocities were set identical to those in Lam et al. (2013). Since NO and NO_2 were separately measured, they were not treated as a whole (i.e. NO_x) in the model. Instead, both NO and NO_2 data were input into the model so that the partitioning between them was constrained to observations.

The simulations were separately performed on all the VOC sampling days. As spin-up, the model was run 72 hours prior to the simulation on the day of interest, with the same inputs. The model treated the air pollutants to be well-mixed within the boundary layer, while dilution and transport were not considered. O_3 in the free troposphere was not considered either, due to the lack of O_3 observations above the boundary layer over Ji'nan. This might hinder the accurate reproduction of the observed O_3, particularly on the days when advection and diffusion were strong. Since the model mainly described the in situ photochemistry, it was validated through comparison with the CHEM process simulated by WRF-CMAQ. The simulated O_3 production rates were output every hour, which were integrated values over every 3600 s in one hour (model resolution: 1 s). More details about the model configuration can be found in Lam et al. (2003) and Lyu et al. (2017).

3. Results and discussion

3.1 Overall characteristics of O_3 pollution in Ji'nan

Figure 2 shows the time series of trace gases, OH reactivity of VOCs, CO and NO_x, and meteorological conditions on the VOC sampling days in Ji'nan (Trace gases in the whole sampling period are shown in Figure S4). All the OH reactivity values discussed in this study were calculated rather than observed ones. The OH reactivity of VOCs was categorized into carbonyls, biogenic VOCs (BVOCs), aromatics, alkenes and alkanes (Table S3 lists the VOCs included in each group). The reaction rate constants between O_3 precursors and OH in calculation of OH reactivity were adopted from the MCM v3.2. The average total OH reactivity on all the VOC sampling days (19.4±2.1 s^{-1}) was comparable to that reported in New York (19±3 s^{-1}, Ren et al., 2003), Houston (9-22 s^{-1}, Mao et al., 2010) and Beijing (15-27 s^{-1}, Williams et al., 2016). Consistent with previous studies in urban areas (Ren et al., 2003; Yang et al., 2016 and references therein), NO_x was the largest contributor (28.9±1.9%) to the total OH reactivity. Noticeably, 20.5±4.1% of the total OH reactivity were attributable to BVOCs, which were much higher than the contributions in urban areas (<10%) reviewed by Yang et al. (2016). The elevated isoprene levels (2.2±0.6 ppbv during episodes and 0.9±0.3 ppbv during non-episodes) under high temperature (mean: 31 °C) explained the considerable contribution of BVOCs to the total OH reactivity in this study.

The total OH reactivity of VOCs and CO ($OH\ reactivity_{VOCs+CO}$) was comparable between O_3 episodes (14.8±2.0 s^{-1}) and non-episodes (12.2±3.0 s^{-1}), so was the OH reactivity of NO_x (4.7±0.8 s^{-1} and 6.9±1.9 s^{-1} during episodes and non-episodes, respectively). Taking the positive biases of NO_2 measurement into account (section 2.2.1), we found that the OH reactivity of NO_x was overestimated at maximum by 17.5±1.1% and 5.4±0.7% during O_3 episodes and non-episodes, respectively. In the case of maximum overestimation, the actual OH reactivity of NO_x during episodes (4.0±0.7 s^{-1}) might be lower ($p<0.05$) than that during non-episodes (6.6±1.9 s^{-1}). The high OH reactivity during non-episodes mainly occurred on July 30 and August 1, due to the unfavorable meteorological conditions, which were discussed later. Despite the comparable OH reactivity, we found that the ratio of $\frac{OH\ reactivity_{VOCs+CO}}{OH\ reactivity_{NOx}}$ during O_3 episodes (3.7±0.7 s^{-1}/s^{-1}) was higher than during non-episodes (2.0±0.4 s^{-1}/s^{-1}) ($p<0.05$). The difference was likely even larger, due to the more significant overestimation of NO_2 during episodes. This indicated that O_3 formation was more limited by VOCs during non-episodes than during episodes. Indeed, O_3 formation in Ji’nan switched from the VOC-limited regime during non-episodes to the transitional regime during episodes (see section 3.4.2). This partially explained the build-up of O_3 on episode days, because the transitional regime features the highest O_3 production rates.

From the aspect of meteorological conditions, O_3 episodes had relatively stronger solar radiation, higher temperature, lower relative humidity and weaker winds ($p<0.05$). This is reasonable as O_3 formation and accumulation are generally enhanced under these weather conditions. In particular, the solar radiation on July 30 was much weaker than those during O_3 episodes, primarily accounting for the low O_3 on this day. Figure S5 shows the COD retrieved from the terra/MODIS (https://ladsweb.modaps.eosdis.nasa.gov/search/imageViewer/1/MOD06_L2--61/2017-08-06/DB/Site:142/2873994172--3) at 10:00 – 12:00 LT on all the VOC sampling days. The terra/MODIS image revealed thick cloud cover with high COD over Ji'nan on July 30, which caused the weak solar radiation. The influences of cloud cover/COD and solar radiation on O_3 pollution were further discussed in section 3.2. Unlike our previous understanding that O_3 pollution is aggravated under high pressure (Chan and Chan, 2000; Zhao et al., 2009), the sea-level pressure during O_3 episodes (993.4±0.2 hPa) was significantly lower than during non-episodes (996.1±0.4 hPa) in this study ($p<0.05$). When O_3 reached its hourly maximum on August 10 (154.1 ppbv), the pressure was at its lowest value (990.2 hPa). This discrepancy inspired us to look into the synoptic and chemical processes in this continuous O_3 pollution event.

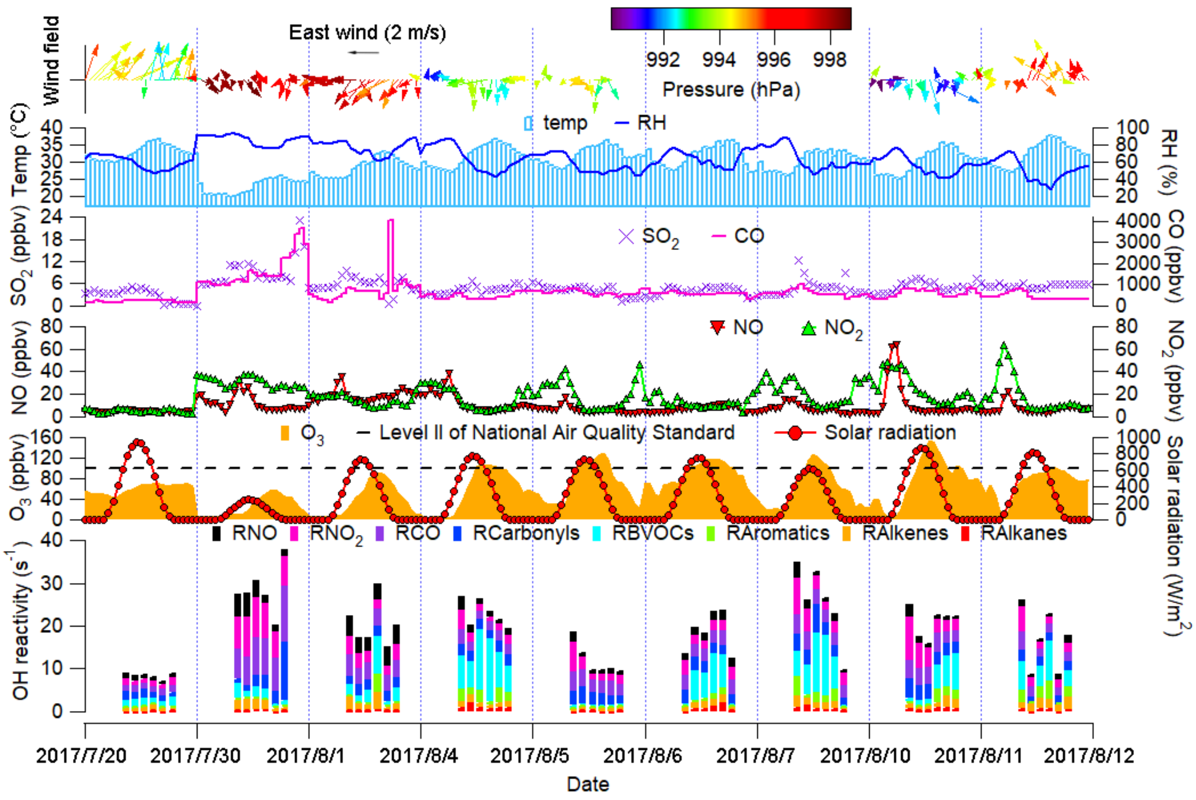

Figure 2 Time series of trace gases, OH reactivity of O_3 precursors and meteorological parameters. Wind speed and wind direction were not monitored from 17:00 LT on August 5 to 23:00 LT on August 7 due to malfunction of the weather station. RX in the bottom panel is the OH reactivity of species/group X.

3.2 Synoptic processes and relationship with O_3 pollution

Figure 3 displays the average weather charts at 14:00 LT during O_3 episodes and non-episodes (weather charts on individual VOC sampling days are shown in Figure S6). Clearly, the temperature in Shandong province was much higher during O_3 episodes than non-episodes, which favored O_3 formation on episode days. Additionally, southerly and southwesterly winds originating from the inland areas (Hubei, Henan, and Anhui provinces) prevailed in central and western Shandong during O_3 episodes. In contrast, the winds were generally from the sea or coastal regions in Jiangsu province during non-episodes. It is more likely that O_3 and O_3 precursors were transported to Ji’nan during episodes. The high concentrations of O_3 precursors on July 30 and August 1 (non-episode days) were mainly caused by the weather conditions (high pressure, low temperature and low solar radiation), as discussed in section 3.1. Further, we also noticed that the winds changed direction from the southwest to the northwest around Ji’nan during O_3 episodes. This meant that there might be a local circulation, hampering the dispersion of air pollutants during episodes. It seemed that the change of wind direction was caused by the convergence of continental air and sea breeze from Bohai Bay, similar to the convergence zone formed over the Pearl River Estuary in South China (Fung et al., 2005; Lo et al., 2006). Overall, the surface winds were more favorable for regional transport and accumulation of air pollutants during O_3 episodes. In addition, Shandong province was under the control of a uniform pressure system with the sea-level pressure of 1000-1001 hPa during O_3 episodes, implying the relatively stagnant weather.

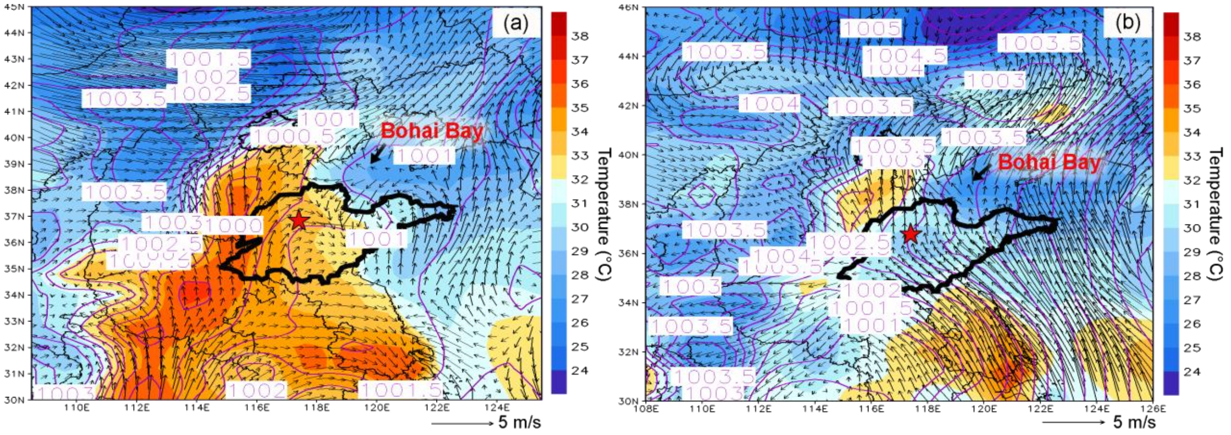

Figure 3 Weather chart at 14:00 LT averaged over (a) O_3 episodes and (b) non-episodes. The red star represents Ji’nan. The dark black line is the boundary of Shandong province. Bohai Bay is

located to the northeast of Shandong province. Numbers in the figure are sea-level pressures in unit of hPa.

To better understand the relationship between O_3 pollution and the synoptic systems, Table 1 summarizes the synoptic systems, weather conditions and air mass origins on all the VOC sampling days. The weather charts at surface level and 500 hPa on August 1, 4, 7, 10 and 13 are presented in Figures S7-S8, showing the evolution of the synoptic systems. To identify the origins of air masses, the backward trajectories of air masses are shown in Figure 4. The trajectories were computed using the Hybrid Single Particle Lagrangian Integrated Trajectory (HYSPLIT) Model v 4.9. Each trajectory was calculated for 48 hours and the calculation was done every 6 hours (4 trajectories each day). Our sampling site (36.68 °N, 117.07 °E) was set as the end point of the trajectories with the height of 500 m a.s.l. The discrepancy between the wind direction and origin of air masses, *e.g.* on August 1 and 11, was likely due to the air recirculation at the ground level.

It was found that Ji'nan was under the control of the Western Pacific Subtropical High (WPSH) on July 20 (weather chart on 500 hPa is not shown here), and the air masses arriving in Ji'nan originated from South China (Figure 4). As anticipated, the WPSH caused high temperature and the intensive solar radiation (Figure 2), which was conducive to O_3 formation. However, the winds on July 20 were the strongest in the entire VOC sampling period, with the highest hourly wind speed of 3.9 m/s. The strong winds facilitated the dispersion of O_3 and its precursors, leading to low O_3 levels on this day. The WPSH moved southward on the following days and Ji'nan was controlled by a uniform pressure system, which was formed in the peripheries of two low pressure systems (two rain belts as shown in Figure 1), *i.e.* one over Central China and another over North China (Figure S7). Thus, the pressure in Ji'nan was relatively high (997.1±0.3 hPa), compared to the south and north regions. This synoptic system lasted for several days until August 7, covering 2 non-episode days and 4 O_3 episode days. The low O_3 on 2 non-episode days (July 30 and August 1) were mainly attributable to the weak solar radiation and low temperature as discussed above.

In contrast, continuously strong solar radiations with low COD (Figure 2 and Figure S5), high temperature and continental air masses (Figure 4) were observed on August 4-7. This, in addition to the shift of O_3 formation mechanism (see sections 3.1 and 3.4.2), explained the prolonged O_3

pollution event. On August 10, the rain belt over North China moved southward, forming a deep low pressure trough over the NCP and Ji'nan was behind the trough (Figure S8 (d)). The low pressure trough is a typical synoptic system conducive to O_3 pollution, resulting from the intrusion of O_3 in the stratosphere and/or the upper troposphere (Chan and Chan, 2000). Moreover, there was nearly no cloud cover over the entire NCP on August 10 (Figure S5). Consequently, the highest O_3 (154.1 ppbv) in this sampling campaign was observed. On August 11, the low pressure system continued to extend to the Yellow Sea. O_3 decreased substantially on this day with the disappearance of the low pressure trough and the weakening of solar radiation, though the hourly maximum O_3 still reached 100.4 ppbv. On the following days, the precipitations relieved the O_3 pollution in Ji'nan.

Table 1 Summary of the synoptic systems, weather conditions and air mass origins on VOC sampling days.

Date	Maximum hourly O_3 (ppbv)	Episode/non-episode	Synoptic system Weather condition	Air mass origin
July 20	71.0	Non-episode	WPSH, strong southwesterly winds	Continental air masses from South China
July 30	57.6		Uniform pressure field (weak high pressure), rain, fog, calm winds	Marine air masses
August 1	90.6		Uniform pressure field (weak high pressure), northeasterly winds	
August 4	107.5	Episode	Uniform pressure field (weak high pressure), northeasterly winds	Continental air masses from Shandong province
August 5	128.2		Uniform pressure field (weak high pressure), calm winds	
August 6	116.9		Uniform pressure field (weak high pressure), southwesterly winds	
August 7	126.9		Uniform pressure field (weak high pressure), calm winds	Continental air masses from the north
August 10	154.1		Low-pressure trough, calm winds	Continental air masses from the west

August 11	100.4	Subtropical high, southeasterly winds	Continental air masses from the southwest

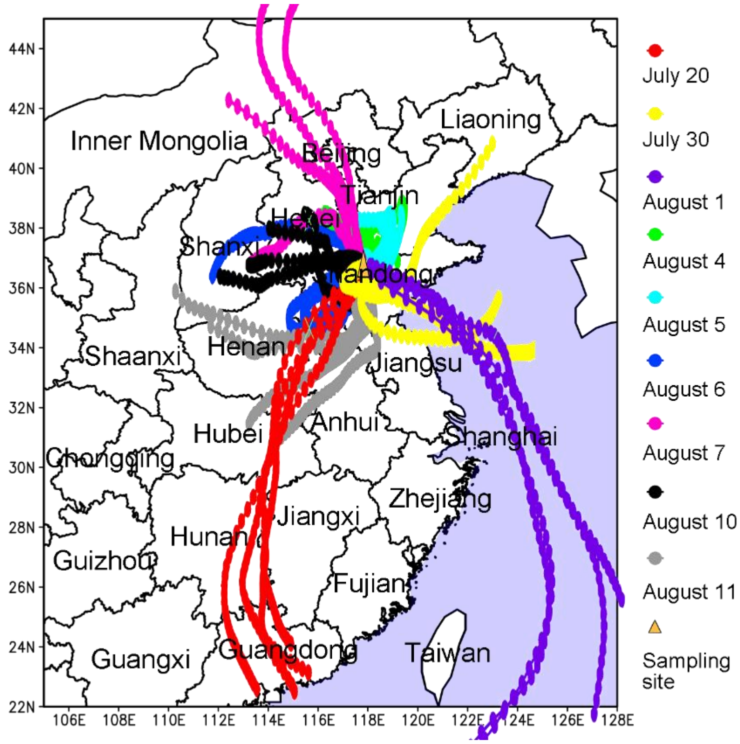

Figure 4 Forty eight hour backward trajectories calculated every 6 hours, with Ji’nan (36.68 °N, 117.07 °E, 500 m a.g.l.) as the ending point. The trajectories are simulated by HYSPLIT v4.9. The water areas are highlighted in blue.

3.3 O_3 simulation and process analysis

The observations indicated the likely different regimes controlling local O_3 formation and the potential impacts of regional transport. To understand the atmospheric chemistry and dynamics, as well as their roles in this O_3 pollution event, the WRF-CMAQ was applied. Figure 5 shows the hourly average simulated and observed O_3 on the VOC sampling days in Ji’nan. Overall, the model well reproduced the magnitudes and diurnal patterns of the observed O_3, except for the higher simulated O_3 on July 20 and the under-prediction of O_3 on August 1, 7 and 10. Discussions on the discrepancies and the model validation were provided in Text S1, Figures S9-S11 and Table S4.

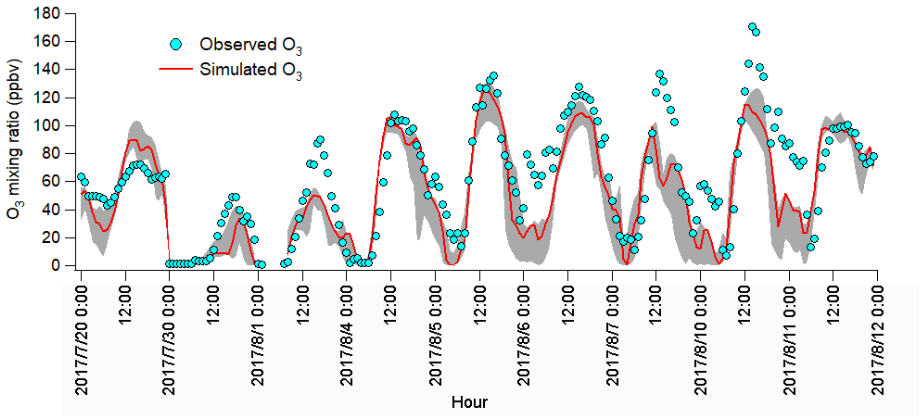

Figure 5 Hourly average mixing ratios of the WRF-CMAQ simulated and observed O_3 in Ji'nan. The grey area shows the minimum and maximum simulated O_3 at the sampling site and 8 adjoining grids (12×12 km^2 for each grid).

The IPR analysis quantified the O_3 variation rates induced by different processes, as shown in Figure 6. HDIF and HADV were summed as horizontal transport (HTRA), and the vertical transport (VTRA) was a total representative of VDIF and VADV. It was found that chemical reactions generally led to the decrease of O_3 mixing ratio during non-episodes. The negative contributions of chemical reactions on July 20 coincided with the very low concentrations of O_3 precursors and the flat diurnal cycle of O_3 (Figure 2). The chemical destruction to O_3 on July 30 and August 1 was most likely related to the weak solar radiation and low temperature, which inhibited the photochemical reactions. In fact, the negative chemical effect should be considered as the titration of NO to the regionally-transported and/or background O_3 and the depletion of O_3 by the freshly emitted NO near the sources (Beck and Grennfelt, 1994; Sillman, 1999). Conversely, the combined effect of horizontal and vertical transport was to increase O_3 levels during non-episodes.

During O_3 episodes, chemical reactions made positive contributions to O_3 production rates between 09:00 LT and 15:00 LT, with the average hourly O_3 production rate of 14.0±2.3 ppbv/hr. At the same time, O_3 was also elevated by transport at an average rate of 18.7±4.0 ppbv/hr, as a combined effect of vertical transport (-40.8±20.2 ppbv/hr) and horizontal transport (59.5±19.8 ppbv/hr). The negative contribution of vertical transport to O_3 in these hours might be caused by the updraft with the increase of temperature in the city. The positive contributions of horizontal transport could be explained by the air masses laden with O_3 originating from the west and the north (Figure 4 and Figure S10). The much higher O_3 over the NCP than in the surrounding regions indicated that the NCP was an O_3 source in this case. In fact, the transport of O_3 from the lower troposphere over the NCP to the free troposphere and further to northeast China was also presented by Ding et al. (2009).

During 16:00-08:00 LT on O_3 episode days, O_3 was titrated and chemically consumed at the rate of 49.4±6.3 ppbv/hr. This was reasonable, because the fresh vehicular emissions in the morning and evening rush hours consumed O_3, particularly the irreversible titration of NO to O_3 in absence of sunlight. The NO_2 produced from the titration reaction was carried over to the other places by air circulation, and/or oxidized to NO_3 and N_2O_5, which could further react with aerosol to form HNO_3 and $ClNO_2$ in the evening. Horizontal and vertical transport dominated O_3 sources, with the average positive contribution of 5.7±7.0 and 54.5±9.6 ppbv/hr during 16:00-08:00 LT on August 4-11, respectively. The strong vertical transport coincided with the downward winds in the evening, which brought the high-altitude O_3 to the ground, as indicated in Figure S9. However, the sources of O_3 in the upper atmosphere were beyond the scope of this study.

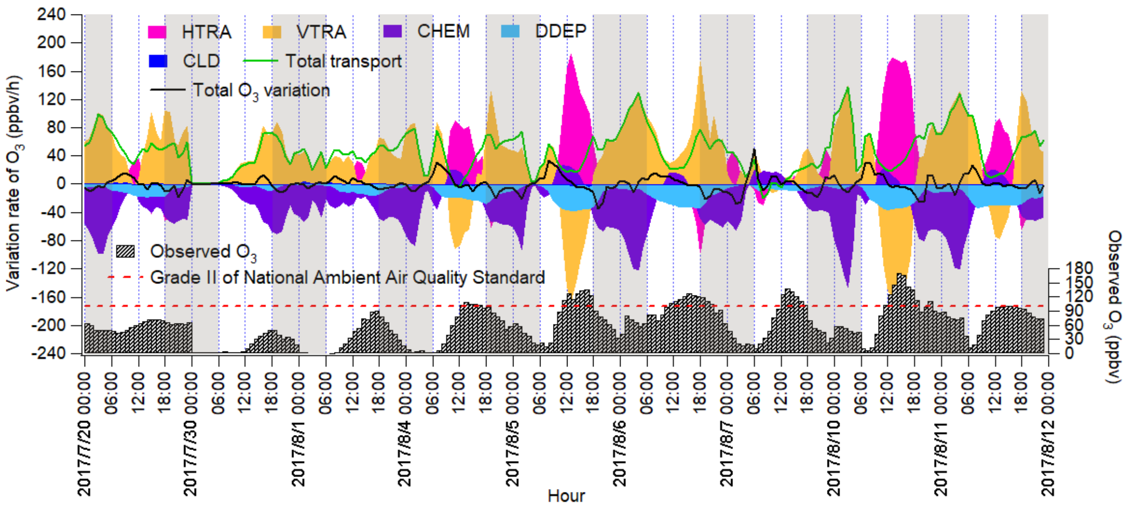

Figure 6 Time series of O_3 variation rate in Ji'nan induced by individual processes calculated based on the change of O_3 per hour. Total transport is the sum of HTRA and VTRA, and the sum of O_3 variation rates attributable to all the processes is represented by total O_3 variation rate. The nighttime (18:00 – 06:00 LT) has been highlighted in grey.

3.4 Local O_3 formation and control

3.4.1 Pathway and source contributions to O_3 production

The IPR analyses showed that chemical reactions served as an important source of O_3 on episode days in Ji'nan, particularly during 09:00-15:00 LT when O_3 was at high levels. This process was further studied through the simulation of the in-situ photochemistry by PBM-MCM. It should be noted that the simulations were based on the observed concentrations of O_3 precursors, which could be influenced by both local and regional air. It required cautions to extend the results to all the situations in Ji'nan, because the regional effect was not always consistent. Table S5 lists the production and destruction pathways of O_3 (Thornton et al., 2002; Monks, 2005; Kanaya et al., 2009). Briefly, the oxidation of NO by HO_2 and RO_2 produced NO_2, which led to O_3 formation following NO_2 photolysis (R2 and R4-R5 in introduction). Therefore, the reactions between NO and HO_2/RO_2 were considered as the production pathways of O_3. To account for O_3 destruction, reaction between $O^1(D)$ and H_2O denoted the photolysis of O_3, and reactions of O_3 with OH, HO_2 and alkenes were also included. Furthermore, since HNO_3 was an important sink of NO_2, the reaction between OH and NO_2 was treated to be destructive to O_3. The titration of O_3 by NO was not included in O_3 destruction, because NO_2 produced in this reaction was either not considered as a source of O_3.

Figure 7 (a) and (b) show the average diurnal cycles of the simulated contributions to O_3 production rates of different pathways. Also shown are the net O_3 production rates simulated by PBM-MCM (*O_3 production $_{PBM\text{-}MCM}$*), those simulated by WRF-CMAQ (*O_3 production $_{CHEM}$*), and those calculated from the observed hourly O_3 (*O_3 production $_{obs.}$*). Overall, *O_3 production $_{PBM\text{-}MCM}$* and *O_3 production $_{obs.}$* were on the same magnitudes, especially during O_3 episodes with more stagnant weather conditions. This indicated that the PBM-MCM model reasonably reproduced the in situ O_3 photochemistry. Though obvious discrepancies existed between *O_3 production $_{CHEM}$* and *O_3 production $_{PBM\text{-}MCM}$*, they agreed well with each other during 10:00-15:00 LT on episode days, consistent with the finding that chemical reactions made great contributions to O_3 in these hours (Figure 6). The lower or even negative *O_3 production $_{CHEM}$* resulted from the titration of the regionally transported and/or local background O_3 by NO and the following depletion of NO_2 through reacting with OH and/or dispersion. Differently, PBM-MCM did not consider the transport of O_3, though the transport effect was partially represented by constraining the model to the observed concentrations of O_3 precursors. In addition, the PBM-MCM was constructed by the observed air pollutants, which were already subject to chemical reactions before being detected by the analytical instruments. This meant that the reaction between NO and O_3 from the emission to the detection of NO_x was not considered in PBM-MCM. However, as an emission-based model, WRF-CMAQ performed better in describing the reactions immediately after the emissions of air pollutants. Therefore, the chemical destructions of O_3 in the vicinity of NO_x sources also accounted for the aforementioned discrepancy. The obviously higher reaction rates between NO and O_3 simulated by WRF-CMAQ (Figure S12) confirmed our inferences.

During both O_3 episodes and non-episodes, the reaction between HO_2 and NO dominated over "RO_2+NO" in O_3 production, while the O_3 destruction was mainly attributable to the formation of HNO_3, the reaction between O_3 and HO_2 and photolysis of O_3. The net O_3 production rate during O_3 episodes (maximum: 21.3 ppbv/hr) was much ($p<0.05$) higher than during non-episodes (maximum: 16.9 ppbv/hr), which partially explained the higher O_3 on episode days. In general, "OH+NO_2" serves as the chain terminating reaction in VOC-limited regime of O_3 formation, while the radical-radical reactions take over the role in NO_x-limited regime (Finlayson-Pitts and Pitts, 1993; Kleinman, 2005). Here, we found that the ratio of total reaction rates between "HO_2+RO_2" and "OH+NO_2" substantially increased from 0.2±0.1 during non-episodes to 1.0±0.3 during O_3 episodes ($p<0.05$). This suggested that O_3 formation during non-episodes was limited by VOCs, while it switched to be co-limited by VOCs and NO_x during O_3 episodes in view of the equivalent role of "HO_2+RO_2" and "OH+NO_2" in terminating the chain reactions.

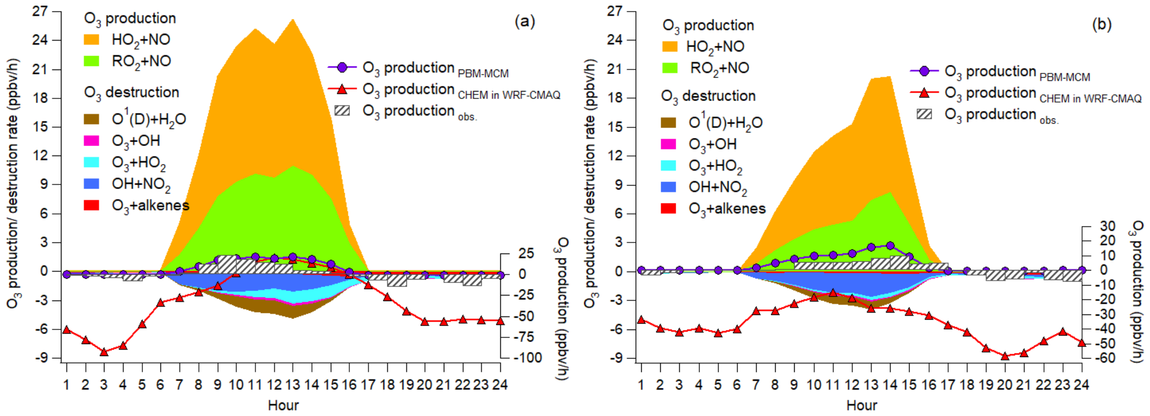

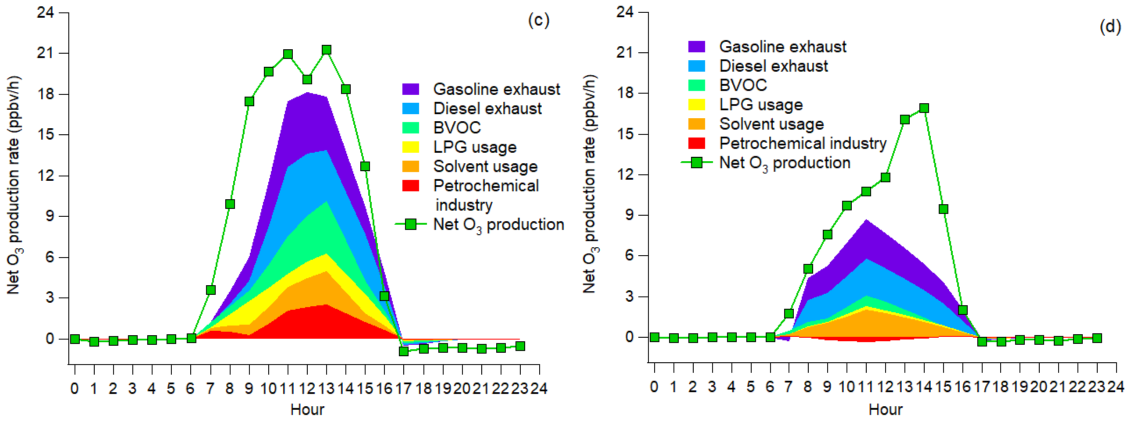

Figure 7 Pathway contributions to O_3 production and destruction rate during episodes (a) and non-episodes (b). Contributions of O_3 precursor sources to net O_3 production rate during episodes (c) and non-episodes (d).

Further, the contributions to the net O_3 production rates of different sources of O_3 precursors were identified, as presented in Figure 7 (c) and (d). Text S2 and Figure S13 illustrate the source apportionment of O_3 precursors and the simulations of the source-specific contributions to O_3 production rates. The results are presented in Table 2. Since the source apportionment was performed for the ambient O_3 precursors which were already subject to atmospheric processes, such as dispersion, deposition and chemical reactions, the results represented the source contributions to the steady – state concentrations of O_3 precursors and the corresponding O_3 production rates. It was found that gasoline exhaust and diesel exhaust were the largest contributors to O_3 production rates regardless of O_3 episodes or non-episodes. Further, the net O_3 production rates attributable to gasoline exhaust (diesel exhaust) increased from 1.0±0.3 ppbv/hr (1.0±0.3 ppbv/hr) during non-episodes to 1.8±0.6 ppbv/hr (1.7±0.4 ppbv/hr) during O_3 episodes. This suggested that vehicular emissions played critical roles in building up ground-level O_3 in the O_3 pollution event. If carbonyls were taken into account, the contributions of vehicular emissions to O_3 production rates were even higher than the currently simulated values, due to the abundances of carbonyls in vehicle exhausts (Grosjean et al., 1990; Granby et al., 1997). In addition, the contributions of the other sources to O_3 production rates all increased during O_3 episodes except for solvent usage (p>0.05), as listed in Table 2. It is not surprising to see the synchronous increases, because of the stronger solar radiation and higher temperature during episodes.

Further insight into the percentage contributions (not shown here) found that the contributions of BVOC, LPG usage and petrochemical industry to O_3 production rates increased substantially from 9.9±4.2%, 4.3±1.4% and -2.8±1.9% during non-episodes to 19.2±4.3%, 9.1±3.4% and 12.1±3.1% during O_3 episodes, respectively. The increased O_3 production rates by BVOCs could be explained by the increase of isoprene (episodes: 2.2±0.6 ppbv; non-episodes: 0.9±0.3 ppbv), under higher temperature and stronger solar radiation during O_3 episodes. The enhancement of O_3 production rates driven by petrochemical industry on episode days was likely associated with the dominance of continental air (Figure 4) and the extensive petrochemical industries in the NCP. For example, the mixing ratio of styrene increased from 54.7±22.0 pptv during non-episodes to 162.3±44.7 pptv during O_3 episodes. The reason for elevated O_3 production rates resulting from LPG usage during episodes was unknown. It is worth to note that the source contributions to O_3 production rates might have some uncertainties due to the limited number of samples (54 samples) and O_3 precursors (31 VOCs, CO, NO and NO_2) applied for source apportionment.

Table 2 Contributions to VOCs, CO, NO, NO_2 and O_3 production rate by the sources of O_3 precursors averaged on the VOC sampling days in Ji'nan (Unit: % unless otherwise specified).

Source	VOCs*	CO	NO	NO_2	O_3 production rate (ppbv/hr)	
					O_3 episodes	Non-episodes
GE [1]	25.7±3.6	29.9±2.1	30.9±2.4	22.2±2.4	1.8±0.6	1.0±0.3
DE [2]	17.6±2.4	57.3±5.2	52.0±5.8	54.4±5.8	1.7±0.4	1.0±0.3
BVOC	6.1±2.6	0.0±1.7	0.0±2.8	0.0±2.3	1.2±0.5	0.2±0.1
LPG [3]	14.7±2.0	2.2±1.1	9.1±1.6	4.7±0.9	0.8±0.5	0.1±0.1
Solvent [4]	17.1±3.9	3.1±1.8	5.1±3.8	7.8±3.1	0.8±0.5	0.7±0.3
PI [5]	18.8±3.1	7.4±1.9	2.9±1.8	10.9±2.5	1.0±0.3	-0.1±0.1

VOCs*: VOCs applied in source apportionment (see Text S2).

[1] gasoline exhaust, [2] diesel exhaust, [3] LPG usage, [4] solvent usage and [5] petrochemical industry.

3.4.2 O_3 control measures

Both WRF-CMAQ and PBM-MCM revealed the significant local O_3 formation in the O_3 pollution event. The relationships between O_3 and its precursors needed to be clarified, so that the science-based control measures could be taken. Throughout the VOC sampling period, the

OH reactivity values of VOCs ($OH\ reactivity_{VOCs}$) were within the range of 33-123% of the average $OH\ reactivity_{VOCs}$ during O_3 episodes. For OH reactivity of NO_x ($OH\ reactivity_{NOx}$), the range was 61-242%. The O_3 production rates were simulated in a set of assumed scenarios with different $OH\ reactivity_{VOCs}$ and $OH\ reactivity_{NOx}$ values. To include the OH reactivity of VOCs and NO_x on all the VOC sampling days, factors from 10% to 140% with the step of 10% were applied to the average diurnal profiles of VOCs and CO during O_3 episodes, while the factors ranged from 10% to 300% with the step of 10% for NO_x. The initial concentrations of all the air pollutants were also scaled by the factors and the model was constrained to these scaled concentrations every hour, except for O_3. It should be noted that the factors applied to CO were exactly the same as those applied to VOCs, therefore we use VOCs$^{\#}$ to represent the sum of VOCs and CO hereafter. The 14 gradients of $OH\ reactivity_{VOCs^{\#}}$ values and 30 gradients of $OH\ reactivity_{NOx}$ values made up 420 scenarios. Meteorological conditions were exactly the same for all the scenarios and the clear sky was hypothesized. According to the simulations, the maximum O_3 production rates occurred at 12:00 LT. Thus, the simulated O_3 production rates at 12:00 LT, as a function of percentages of $OH\ reactivity_{VOCs}$ and $OH\ reactivity_{NOx}$, are plotted in Figure 8.

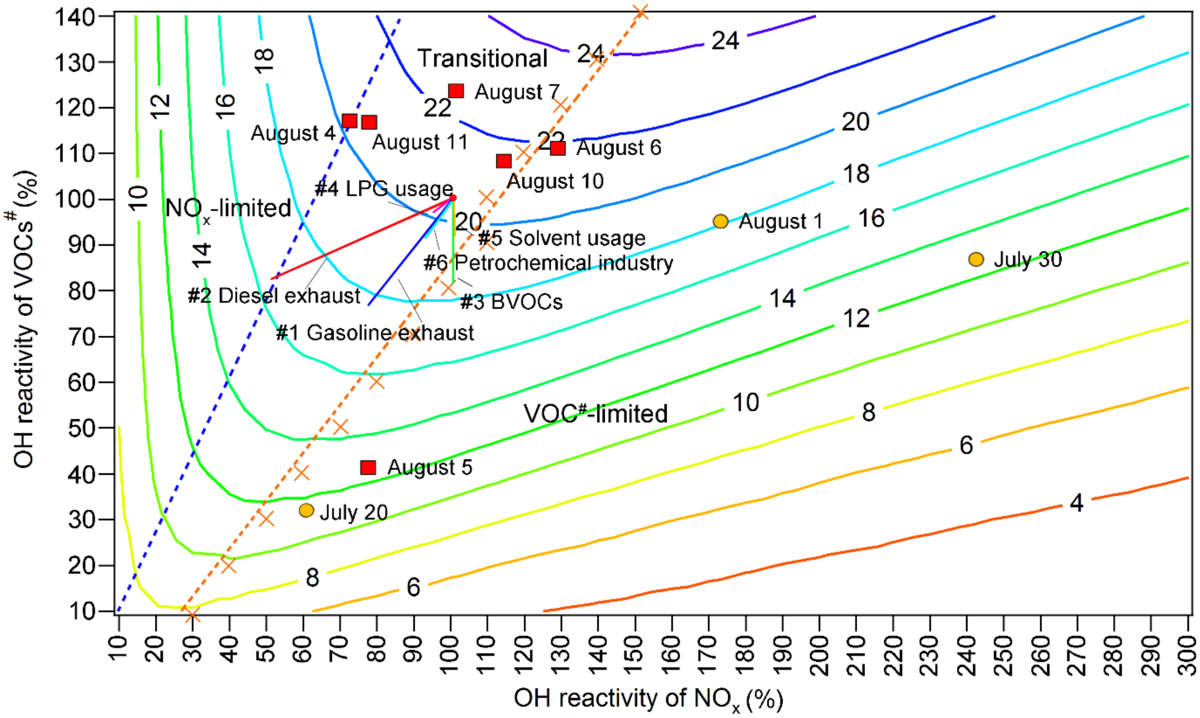

Figure 8 Isopleths of the net O_3 production rate (ppbv/hr) at 12:00 LT as a function of $OH\ reactivity_{VOCs^{\#}}$ and $OH\ reactivity_{NOx}$. The red blocks and orange circles denote the calculated $OH\ reactivity_{VOCs^{\#}}$ and $OH\ reactivity_{NOx}$ values at 12:00 LT on O_3 episode and non-episode days, respectively. Each orange cross represents the $OH\ reactivity_{VOCs^{\#}}$ and $OH\ reactivity_{NOx}$ at 12:00 LT in the scenario with highest O_3 production rate at a given $OH\ reactivity_{VOCs^{\#}}$. The orange dashed line and blue dashed line divide O_3 formation into the VOC-limited regime, transitional regime, and NO_x-limited regime.

Text S3 describes the methods to define the regimes of O_3 formation. Overall, O_3 formation was mainly limited by VOCs$^{\#}$ during non-episodes. However, it switched to be co-limited by VOCs$^{\#}$ and NO_x (transitional regime) on episode days with the net O_3 production rates among the highest, except for August 5 when the strong sea breeze diluted air pollutants in Ji'nan and/or intercepted the transport of air pollutants from Central China to Ji'nan (Figure S6). In fact, the sensitivity of O_3 formation to NO_x might be underemphasized due to the positive biases of NO_2 measurement (Lu et al., 2010). This effect was expected to be more significant during episodes when the overestimation of NO_2 was more obvious. However, O_3 formation was not likely only limited by NO_x even during O_3 episodes, because NO_2 could not be overestimated by more than 30% according to our inferences (see section 2.2.1). Therefore, O_3 formation was treated to be in the transitional regime during episodes. This partially explained the increased O_3 during episodes in Ji'nan, given the higher O_3 production rates in transitional regime (Figure 8). Noticeably, the change of regimes controlling O_3 formation is consistent with that predicted by the $\frac{OH\ reactivity_{VOCs^{\#}}}{OH\ reactivity_{NOx}}$ ratio and the ratio of the reaction rates between "HO_2+RO_2" and "OH+NO_2".

The source apportionment of O_3 precursors enabled us to calculate the source-specific $OH\ reactivity_{VOCs^{\#}}$ and $OH\ reactivity_{NOx}$ values. Accordingly, the variations of O_3 production rates induced by the reductions in source emissions are presented in Figure 8 (straight solid lines #1-#6). The start point of the straight lines corresponded to 100% of the total average $OH\ reactivity_{VOCs^{\#}}$ and $OH\ reactivity_{NOx}$ during O_3 episodes. The end points, however, represented the $OH\ reactivity_{VOCs^{\#}}$ and $OH\ reactivity_{NOx}$ with the complete removal of emissions from the individual sources. Therefore, the differences of the O_3 production rates between the start point and end points were the source contributions to the O_3 production rates, while the lengths of the lines reflected the contributions to the OH reactivity of the sources. Further, the simulated O_3 production rates on the lines #1-#6, as a response of reductions in source emissions, are extracted and plotted in Figure S14. Obviously, the highest efficiencies of O_3 reduction could be achieved by cutting diesel exhaust (0.58 ppbv hr^{-1}/10% emission reduction) and gasoline exhaust (0.47 ppbv hr^{-1}/10% emission reduction). In fact, the sensitivities of O_3 production rates to the vehicle exhausts might be somewhat underestimated, due to the exclusion of carbonyls in the source apportionment. However, the reductions of O_3 production rates by cutting 10% of vehicle exhausts were still insignificant, compared to the overall maximum O_3 production rate of 21.3 ppbv/hr during O_3 episodes. This indicated that by only restraining emissions from one to two sources, high percentages of emission reductions were required to sufficiently reduce the overall O_3 production rate. Otherwise, the combined efforts should be made to control the emissions of O_3 precursors from the diverse sources. In particular, it is essential to get rid of the transitional regime featuring high O_3 production rates.

4 Implications

This study investigates the causes of a severe O_3 pollution event lasting for eight consecutive days in the NCP, one of the most densely populated regions in the world. Photochemical formation in the lower troposphere of the NCP is demonstrated as the main source of O_3, under the control of weak high pressure or low pressure trough. Though the emissions of NO_x, an important precursor of O_3, have been significantly reduced in China since 2013 (Duncan et al., 2016; Liu et al., 2017), O_3 pollution is still severe or even worsening in the NCP, as revealed in the present and also previous studies (Zhang et al., 2014; Sun et al., 2016). The finding that O_3 formation shifted from VOC-limited regime on relatively low O_3 days to the transitional regime on O_3 non-attainment days may elucidate the increase of O_3, because O_3 production rates in the transitional regime are the highest. It is unrealistic to expect the continuously linear reduction in NO_x emissions in the NCP, after the substantial decreases of emissions from power plants and industries in recent years. In other words, restraining on VOC emissions is urgent for O_3 abatement in the NCP. Another important finding in this study is that the NCP served as an O_3 source. This was ever proposed by Ding et al. (2009), based on the aircraft measurement and simulation of atmospheric dynamics. We confirm it through the ground-level observation and the simulation of in-situ photochemistry. It can be expected that organic nitrates are also intensively formed in the NCP as byproducts of O_3 formation. In view of the fact that the NCP locates within the mid-latitude band of Northern Hemisphere under the dominance of westerlies, we believe that O_3 and organic nitrates formed in this region may be transported over a long distance following the uplifting of air masses, which has been confirmed to partially account for the enhancement of background O_3 in North America and even Europe (Derwent et al., 2015; Lin et al., 2017). Therefore, the recent air pollution control measures taken in China (including China's Clean Air Act Plan in force in 2013) are still inadequate to ease the burden of global tropospheric O_3 in a short period. More effective Action Plans should be implemented for O_3 benefit, with comprehensive thinking of atmospheric dynamics and chemistry.

Author contribution

The study was designed by the corresponding author, Hai Guo, with the help of Lihui Han and Ying Zhou. Fei Jiang and Hairong Cheng provided valuable input on the characteristics of meteorological conditions and emissions of air pollutants in the NCP. Xiaopu Lyu collected the samples and managed the logistics in the field campaign, when Likun Xue provided sufficient assistances in field sampling campaign. The solar radiation data in Ji'nan were obtained from Zhe Cai. Xiaopu Lyu did data analyses and wrote the paper, while the chemical transport modelling was done by Nan Wang and Yangzong Zeren. Hai Guo revised and finalized the paper for submission.

Acknowledgements: This study was supported by the National Key R&D Program of China (2017YFC0212001), the Research Grants Council of the Hong Kong Special Administrative Region via grants PolyU5154/13E, PolyU152052/14E, PolyU152052/16E, CRF/C5004-15E and CRF/C5022-14G, the Collaborative Research program between The Beijing University of Technology and The Hong Kong Polytechnic University (PolyU) (4-ZZFW), the Hong Kong Polytechnic University PhD scholarships (project RTUP), and the National Natural Science Foundation of China (No. 41675118). This study was partly supported by the Hong Kong PolyU internal grant (G-YBUQ, 1-ZVJT and 1-BBW4). The valuable comments of the anonymous reviewers were highly appreciated. The data are accessible at https://drive.google.com/open?id=1_KeOxOuVsLY83xL74RtcRORsiiyIR 8FZ.

References

Atkinson, R.: Atmospheric chemistry of VOCs and NO_x, Atmos. Environ., 34, 2063-2101, **2000**.

Beck, J.P. and Grennfelt, P.: Estimate of ozone production and destruction over northwestern Europe, Atmos. Environ., 28, 129-140, **1994**.

Cai, C., Geng, F., Tie, X., Yu, Q., and An, J.: Characteristics and source apportionment of VOCs measured in Shanghai, China, Atmos. Environ., 44, 5005-5014, **2010**.

Carter, W.P.: Development of ozone reactivity scales for volatile organic compounds, Air & Waste Manage. Assoc., 44, 881-899, **1994**.

Carter, W.P., Pierce, J.A., Luo, D., and Malkina, I.L.: Environmental chamber study of maximum incremental reactivities of volatile organic compounds, Atmos. Environ., 29(18), 2499-2511, **1995**.

Chameides, W. and Walker, J.C.: A photochemical theory of tropospheric ozone, J. Geophys. Res., 78(36), 8751-8760, **1973**.

Chan, C.Y. and Chan, L.Y.: Effect of meteorology and air pollutant transport on ozone episodes at a subtropical coastal Asian city, Hong Kong, J. Geophys. Res. – Atmos., 105(D16), 20707-20724, **2000**.

Chen, Y., Zhao, C., Zhang, Q., Deng, Z., Huang, M., and Ma, X.: Aircraft study of mountain chimney effect of Beijing, China, J. Geophys. Res. – Atmos., 114(D8), doi:10.1029/2008JD010610, **2009**.

Cheng, H., Guo, H., Wang, X., Saunders, S.M., Lam, S.H.M., Jiang, F., Wang, T., Ding, A., Lee, S., and Ho, K.F.: On the relationship between ozone and its precursors in the Pearl River Delta: application of an observation-based model (OBM), Environ. Sci. Pollut. Res., 17(3), 547-560, **2010**.

Colman, J.J., Swanson, A.L., Meinardi, S., Sive, B.C., Blake, D.R., and Rowland, F.S.: Description of the analysis of a wide range of volatile organic compounds in whole air samples collected during PEM-Tropics A and B, Anal. Chem., 73(15), 3723-3731, **2001**.

Cooper, O.R., Stohl, A., Hübler, G., Hsie, E.Y., Parrish, D.D., Tuck, A.F., Kiladis, G.N., Oltmans, S.J., Johnson, B.J., Shapiro, M., and Moody, J.L.: Direct transport of midlatitude stratospheric ozone into the lower troposphere and marine boundary layer of the tropical Pacific Ocean, J. Geophys. Res.: Atmos., 110(D23), **2005**.

Crutzen, P.: A discussion of the chemistry of some minor constituents in the stratosphere and troposphere, Pure Appl. Geophys., 106(1), 1385-1399, **1973**.

Derwent, R.G., Utembe, S.R., Jenkin, M.E., and Shallcross, D.E.: Tropospheric ozone production regions and the intercontinental origins of surface ozone over Europe, Atmos. Environ., 112, 216-224, **2015**.

Ding, A.J., Fu, C.B., Yang, X.Q., Sun, J.N., Zheng, L.F., Xie, Y.N., Herrmann, E., Nie, W., Petaja, T., Kerminen, V.M., and Kulmala, M.: Ozone and fine particle in the western Yangtze River Delta: an overview of 1 yr data at the SORPES station, Atmos. Chem. Phys., 13(11):5813-30, **2013**.

Ding, A., Wang, T., Xue, L., Gao, J., Stohl, A., Lei, H., Jin, D., Ren, Y., Wang, X., Wei, X., and Qi, Y.: Transport of north China air pollution by midlatitude cyclones: Case study of aircraft measurements in summer 2007, J. Geophys. Res.: Atmos., 114(D8), **2009**.

Duncan, B.N., Lamsal, L.N., Thompson, A.M., Yoshida, Y., Lu, Z., Streets, D.G., Hurwitz, M.M., and Pickering, K.E.: A space-based, high-resolution view of notable changes in urban NO_x pollution around the world (2005-2014), J. Geophys. Res.: Atmos., 121(2), 976-996, **2016**.

Dunlea, E.J., Herndon, S.C., Nelson, D.D., Volkamer, R.M., San Martini, F., Sheehy, P.M., Zahniser, M.S., Shorter, J.H., Wormhoudt, J.C., Lamb, B.K., and Allwine, E.J.: Evaluation of nitrogen dioxide chemiluminescence monitors in a polluted urban environment, Atmos. Chem. Phys., 7(10), 2691-2704, **2007**.

Finlayson-Pitts, B.J., and Pitts Jr, J.N.: Atmospheric chemistry of tropospheric ozone formation: scientific and regulatory implications, Air & Waste Manage. Assoc., 43(8), 1091-1100, **1993**.

Fung, J.C.H., Lau, A.K.H., Lam, J.S.L., and Yuan, Z.: Observational and modeling analysis of a severe air pollution episode in western Hong Kong, J. Geophys. Res. – Atmos., 110(D9), **2005**.

Gao, J., Wang, T., Ding, A., and Liu, C.: Observational study of ozone and carbon monoxide at the summit of mount Tai (1534m asl) in central-eastern China, Atmos. Environ., 39(26), 4779-4791, **2005**.

Granby, K., Christensen, C.S., and Lohse, C.: Urban and semi-rural observations of carboxylic acids and carbonyls, Atmos. Environ., 31(10), 1403-1415, **1997**.

Grosjean, D., Miguel, A.H., and Tavares, T.M.: Urban air pollution in Brazil: Acetaldehyde and other carbonyls, Atmos. Environ., 24(1), 101-106, **1990**.

Gu, D., Wang, Y., Smeltzer, C., and Boersma, K.F.: Anthropogenic emissions of NO_x over China: Reconciling the difference of inverse modeling results using GOME-2 and OMI measurements. J. Geophys. Res.: Atmos., 119(12):7732-40, **2014**.

Guo, H., Ling, Z.H., Cheung, K., Jiang, F., Wang, D.W., Simpson, I.J., Barletta, B., Meinardi, S., Wang, T.J., Wang, X.M., Saunders, S.M., and Blake, D.R.: Characterization of photochemical pollution at different elevations in mountainous areas in Hong Kong, Atmos. Chem. Phys., 13(8), 3881-3898, **2013**.

Han, X., Zhu, L., Wang, S., Meng, X., Zhang, M., and Hu, J.: Modeling study of impacts on surface ozone of regional transport and emissions reductions over North China Plain in summer 2015, Atmos. Chem. Phys., 18(16):12207-21, **2018**.

He, J., Wang, Y., Hao, J., Shen, L., and Wang, L.: Variations of surface O_3 in August at a rural site near Shanghai: influences from the West Pacific subtropical high and anthropogenic emissions, Environ. Sci. Pollut. Res., 19(9), 4016-4029, **2012**.

He, K.: Multi-resolution Emission Inventory for China (MEIC): model framework and 1990-2010 anthropogenic emissions, In AGU Fall Meeting Abstracts, December, **2012**.

Huang, J.P., Fung, J.C., Lau, A.K., and Qin, Y.: Numerical simulation and process analysis of typhoon-related ozone episodes in Hong Kong, J. Geophys. Res. – Atmos., 110(D5), **2005**.

Jenkin, M.E. and Clemitshaw, K.C.: Ozone and other secondary photochemical pollutants: chemical processes governing their formation in the planetary boundary layer, Atmos. Environ., 34(16), 2499-2527, **2000**.

Jenkin, M.E., Saunders, S.M., and Pilling, M.J.: The tropospheric degradation of volatile organic compounds: a protocol for mechanism development, Atmos. Environ., 31(1), 81-104, **1997**.

Jiang, F., Guo, H., Wang, T.J., Cheng, H.R., Wang, X.M., Simpson, I.J., Ding, A.J., Saunders, S.M., Lam, S.H.M., and Blake, D.R.: An ozone episode in the Pearl River Delta: Field observation and model simulation, J. Geophys. Res. – Atmos., 115(D22), **2010**.

Jin, X., Fiore, A.M., Murray, L.T., Valin, L.C., Lamsal, L.N., Duncan, B., Folkert Boersma, K., De Smedt, I., Abad, G.G., Chance, K., and Tonnesen, G.S.: Evaluating a Space-Based Indicator of Surface Ozone-NO_x-VOC Sensitivity Over Midlatitude Source Regions and Application to Decadal Trends, J. Geophys. Res.: Atmos., 122(19), **2017**.

Kanaya, Y., Pochanart, P., Liu, Y., Li, J., Tanimoto, H., Kato, S., Suthawaree, J., Inomata, S., Taketani, F., Okuzawa, K., and Kawamura, K.: Rates and regimes of photochemical ozone production over Central East China in June 2006: a box model analysis using comprehensive measurements of ozone precursors, Atmos. Chem. Phys., 9(20), 7711-7723, **2009**.

Kleinman, L.I.: The dependence of tropospheric ozone production rate on ozone precursors, Atmos. Environ., (3), 575-586, **2005**.

Kusaka, H. and Kimura, F.: Coupling a single-layer urban canopy model with a simple atmospheric model: Impact on urban heat island simulation for an idealized case, J. Meteoro. Soc. Japan: Ser. II, 82(1), 67-80, **2004**.

Lam, S.H.M., Saunders, S.M., Guo, H., Ling, Z.H., Jiang, F., Wang, X.M., and Wang, T.J.: Modelling VOC source impacts on high ozone episode days observed at a mountain summit in Hong Kong under the influence of mountain-valley breezes, Atmos. Environ., 81, 166-176, **2013**.

Lang, J., Zhang, Y., Zhou, Y., Cheng, S., Chen, D., Guo, X., Chen, S., Li, X., Xing, X., and Wang, H.: Trends of $PM_{2.5}$ and chemical composition in Beijing, 2000–2015, Aerosol Air Qual. Res., 17, 412-425, **2017**.

Li, M., Zhang, Q., Kurokawa, J.I., Woo, J.H., He, K., Lu, Z., Ohara, T., Song, Y., Streets, D.G., Carmichael, G.R., and Cheng, Y.: MIX: a mosaic Asian anthropogenic emission inventory under the international collaboration framework of the MICS-Asia and HTAP, Atmos. Chem. Phys., 17(2), **2017**.

Lin, M., Fiore, A.M., Horowitz, L.W., Langford, A.O., Oltmans, S.J., Tarasick, D., and Rieder, H.E.: Climate variability modulates western US ozone air quality in spring via deep stratospheric intrusions, Nat. Commun., 6:7105, **2015**.

Lin, M., Horowitz, L.W., Payton, R., Fiore, A.M., and Tonnesen, G.: US surface ozone trends and extremes from 1980 to 2014: quantifying the roles of rising Asian emissions, domestic controls, wildfires, and climate, Atmos. Chem. Phys., 17(4), 2943-2970, **2017**.

Lin, W., Xu, X., Zhang, X., and Tang, J.: Contributions of pollutants from North China Plain to surface ozone at the Shangdianzi GAW Station, Atmos. Chem. Phys., 8(19), 5889-5898, **2008**.

Liu, F., Beirle, S., Zhang, Q., Zheng, B., Tong, D., and He, K.: NO_x emission trends over Chinese cities estimated from OMI observations during 2005 to 2015, Atmospheric chemistry and physics, 17(15), 9261-9275, **2017**.

Liu, X.H., Zhang, Y., Xing, J., Zhang, Q., Wang, K., Streets, D.G., Jang, C., Wang, W.X., and Hao, J.M.: Understanding of regional air pollution over China using CMAQ, part II. Process analysis and sensitivity of ozone and particulate matter to precursor emissions, Atmos. Environ., 44(30), 3719-3727, **2010**.

Lo, J.C., Lau, A.K., Fung, J.C., and Chen, F.: Investigation of enhanced cross-city transport and trapping of air pollutants by coastal and urban land-sea breeze circulations, J. Geophys. Res. – Atmos., 111(D14), **2006**.

Lyu, X.P., Chen, N., Guo, H., Zhang, W.H., Wang, N., Wang, Y., and Liu, M.: Ambient volatile organic compounds and their effect on ozone production in Wuhan, central China, Sci. Total Environ., 541:200-9, **2016**.

Lyu, X.P., Guo, H., Wang, N., Simpson, I.J., Cheng, H.R., Zeng, L.W., Saunders, S.M., Lam, S. H.M., Meinardi, S., and Blake, D.R.: Modeling C_1-C_4 alkyl nitrate photochemistry and their impacts on O_3 production in urban and suburban environments of Hong Kong, J. Geophys. Res. – Atmos., 122(19), **2017**.

Lu, K., Zhang, Y., Su, H., Brauers, T., Chou, C.C., Hofzumahaus, A., Liu, S.C., Kita, K., Kondo, Y., Shao, M., and Wahner, A.: Oxidant (O_3 + NO_2) production processes and formation regimes in Beijing, J. Geophys. Res.: Atmos., 115(D7), **2010**.

Madronich, S. and Flocke, S.: Theoretical estimation of biologically effective UV radiation at the Earth's surface, In Solar Ultraviolet Radiation (pp. 23-48), Springer, Berlin, Heidelberg, **1997**.

Mao, J., Ren, X., Chen, S., Brune, W.H., Chen, Z., Martinez, M., Harder, H., Lefer, B., Rappenglueck, B., Flynn, J., and Leuchner, M.: Atmospheric oxidation capacity in the summer of Houston 2006: Comparison with summer measurements in other metropolitan studies, Atmos. Environ., 44(33), 4107-4115, **2010**.

McClenny, W.A., Williams, E.J., Cohen, R.C., and Stutz, J.: Preparing to measure the effects of the NO_x SIP Call—methods for ambient air monitoring of NO, NO_2, NO_y, and individual NO_z species, Air & Waste Manage. Assoc,, 52(5), 542-562, **2002**.

Monks, P. S.: Gas-phase radical chemistry in the troposphere, Chem. Soc. Reviews, 34(5), 376-395, **2005**.

Ren, X., Harder, H., Martinez, M., Lesher, R.L., Oliger, A., Simpas, J.B., Brune, W.H., Schwab, J.J., Demerjian, K.L., He, Y., and Zhou, X.: OH and HO_2 chemistry in the urban atmosphere of New York City, Atmos. Environ., 37(26), 3639-3651, **2003**.

Saunders, S.M. Jenkin, M.E., Derwent, R.G., and Pilling, M.J.: Protocol for the development of the Master Chemical Mechanism, MCM v3 (Part A): tropospheric degradation of non-aromatic volatile organic compounds, Atmos. Chem. Phys., 3(1), 161-180, **2003**.

Shan, W., Yin, Y., Zhang, J., and Ding, Y.: Observational study of surface ozone at an urban site in East China, Atmos. Res., 89(3), 252-261, **2008**.

Shao, M., Lu, S., Liu, Y., Xie, X., Chang, C., Huang, S., and Chen, Z.: Volatile organic compounds measured in summer in Beijing and their role in ground-level ozone formation, J. Geophys. Res. – Atmos., 114(D2), doi.org/10.1029/2008JD010863, **2009b**.

Shu, L., Xie, M., Wang, T., Gao, D., Chen, P., Han, Y., Li, S., Zhuang, B., and Li, M.: Integrated studies of a regional ozone pollution synthetically affected by subtropical high and typhoon system in the Yangtze River Delta region, China, Atmos. Chem. Phys., 16(24), 15801-15819, **2016**.

Sillman, S.: The relation between ozone, NO_x and hydrocarbons in urban and polluted rural environments, Atmos. Environ., 33(12), 1821-1845, **1999**.

Sun, L., Xue, L., Wang, T., Gao, J., Ding, A., Cooper, O.R., Lin, M., Xu, P., Wang, Z., Wang, X., Wen, L., Zhu, Y., Chen, T., Yang, L., Wang, Y., Chen, J., and Wang, W.: Significant increase of summertime ozone at Mount Tai in Central Eastern China, Atmos. Chem. Phys., 16(16), 10637-10650, **2016**.

Tan, Z., Lu, K., Dong, H., Hu, M., Li, X., Liu, Y., Lu, S., Shao, M., Su, R., Wang, H., and Wu, Y.: Explicit diagnosis of the local ozone production rate and the ozone-NO_x-VOC sensitivities, Sci. Bull., 63(16):1067-76, **2018**.

Tan, Z., Lu, K., Jiang, M., Su, R., Dong, H., Zeng, L., Xie, S., Tan, Q., and Zhang, Y.: Exploring ozone pollution in Chengdu, southwestern China: A case study from radical chemistry to O_3-VOC-NO_x sensitivity, Sci. Total Environ., 636:775-86, **2018**.

Thornton, J.A., Wooldridge, P.J., Cohen, R.C., Martinez, M., Harder, H., Brune, W.H., Williams, E.J., Roberts, J.M., Fehsenfeld, F.C., Hall, S.R., and Shetter, R.E.: Ozone production rates as a function of NO_x abundances and HO_x production rates in the Nashville urban plume, J. Geophys. Res. – Atmos., 107(D12), doi.org/10.1029/2001JD000932, **2002**.

Wang, N., Guo, H., Jiang, F., Ling, Z. H., and Wang, T.: Simulation of ozone formation at different elevations in mountainous area of Hong Kong using WRF-CMAQ model, Sci. Total Environ., 505, 939-951, **2015b**.

Wang, T., Ding, A., Gao, J., and Wu, W.S.: Strong ozone production in urban plumes from Beijing, China, Geophys. Res. Lett., 33(21), **2006**.

Wang, T., Nie, W., Gao, J., Xue, L.K., Gao, X.M., Wang, X.F., Qiu, J., Poon, C.N., Meinardi, S., Blake, D., Wang, S.L., Ding, A.J., Chai, F.H., Zhang, Q.Z., and Wang, W.X.: Air quality during the 2008 Beijing Olympics: secondary pollutants and regional impact, Atmos. Chem. Phys., 10(16), 7603-7615, **2010**.

Wang, X.M., Lin, W.S., Yang, L.M., Deng, R.R., and Lin, H.: A numerical study of influences of urban land‐use change on ozone distribution over the Pearl River Delta region, China, Tellus B, 59(3), 633-641, **2007**.

Wang, Z., Li, Y., Chen, T., Zhang, D., Sun, F., Wei, Q., Dong, X., Sun, R., Huan, N., and Pan, L.: Ground-level ozone in urban Beijing over a 1-year period: Temporal variations and relationship to atmospheric oxidation, Atmos. Res., 164, 110-117, **2015a**.

Whitten, G.Z., Heo, G., Kimura, Y., McDonald-Buller, E., Allen, D.T., Carter, W.P., and Yarwood, G.: A new condensed toluene mechanism for Carbon Bond: CB05-TU, Atmos. Environ., 44(40), 5346-5355, **2010**.

Williams, J., Keßel, S.U., Nölscher, A.C., Yang, Y., Lee, Y., Yáñez-Serrano, A.M., Wolff, S., Kesselmeier, J., Klüpfel, T., Lelieveld, J., and Shao, M.: Opposite OH reactivity and ozone cycles in the Amazon rainforest and megacity Beijing: Subversion of biospheric oxidant control by anthropogenic emissions, Atmos. Environ., 125, 112-118, **2016**.

Xing, C., Liu, C., Wang, S., Chan, K.L., Gao, Y., Huang, X., Su, W., Zhang, C., Dong, Y., Fan, G., and Zhang, T.: Observations of the vertical distributions of summertime atmospheric pollutants and the corresponding ozone production in Shanghai, China, Atmos. Chem. Phys., 17(23), **2017**.

Xing, J., Ding, D., Wang, S., Zhao, B., Jang, C., Wu, W., Zhang, F., Zhu, Y., and Hao, J.: Quantification of the enhanced effectiveness of NO_x control from simultaneous reductions of VOC and NH_3 for reducing air pollution in the Beijing–Tianjin–Hebei region, China, Atmos. Chem. Phys., 18(11):7799-814, **2018**.

Xu, Z., Wang, T., Xue, L.K., Louie, P.K., Luk, C.W., Gao, J., Wang, S.L., Chai, F.H., and Wang, W.X.: Evaluating the uncertainties of thermal catalytic conversion in measuring atmospheric nitrogen dioxide at four differently polluted sites in China, Atmos. Environ., 76, 221-226, **2013**.

Xue, L.K., Wang, T., Gao, J., Ding, A.J., Zhou, X.H., Blake, D.R., Wang, X.F., Saunders, S.M., Fan, S.J., Zuo, H.C., Zhang, Q.Z. and Wang, W.X.: Ground-level ozone in four Chinese cities: precursors, regional transport and heterogeneous processes, Atmos. Chem. Phys., 14(23), 13175-13188, **2014**.

Yang, Y., Shao, M., Wang, X., Nolscher, A.C., Kessel, S., Guenther, A., and Williams, J.: Towards a quantitative understanding of total OH reactivity: A review, Atmos. Environ., 134:147-161, **2016**.

Ye, L., Wang, X., Fan, S., Chen, W., Chang, M., Zhou, S., Wu, Z., and Fan, Q.: Photochemical indicators of ozone sensitivity: application in the Pearl River Delta, China, Front. Env. Sci. Eng. 10(6):15, **2016**.

Yin, Y., Lu, H., Shan, W., and Zheng, Y.: Analysis of observed ozone episode in urban Jinan, China, Bulletin Environ. Contamination & toxico., 83(2), 159-163, **2009**.

Zhang, Q., Streets, D.G., Carmichael, G.R., He, K.B., Huo, H., Kannari, A., Klimont, Z., Park, I.S., Reddy, S., Fu, J.S., Chen, D., Duan, L., Lei, Y., Wang, L.T., and Yao, Z.L.,: Asian emissions in 2006 for the NASA INTEX-B mission, Atmos. Chem. Phys., 9(14), 5131-5153, **2009**.

Zhang, Q., Streets, D.G., He, K., Wang, Y., Richter, A., Burrows, J.P., Uno, I., Jang, C.J., Chen, D., Yao, Z., and Lei, Y.: NO_x emission trends for China, 1995-2004: The view from the ground and the view from space, J. Geophys. Res. – Atmos., 112(D22), **2007**.

Zhang, Q., Yuan, B., Shao, M., Wang, X., Lu, S., Lu, K., Wang, M., Chen, L., Chang, C.C., and Liu, S.C.: Variations of ground-level O_3 and its precursors in Beijing in summertime between 2005 and 2011, Atmos. Chem. Phys., 14(12), 6089-6101, **2014**.

Zhang, Y., Ding, A., Mao, H., Nie, W., Zhou, D., Liu, L., Huang, X., and Fu, C.: Impact of synoptic weather patterns and inter-decadal climate variability on air quality in the North China Plain during 1980-2013, Atmos. Environ., 124, 119-128, **2016**.

Zhang, Z., Zhang, X., Gong, D., Quan, W., Zhao, X., Ma, Z., and Kim, S.J.: Evolution of surface O_3 and $PM_{2.5}$ concentrations and their relationships with meteorological conditions over the last decade in Beijing, Atmos. Environ., 108, 67-75, **2015**.

Zhao, C., Wang, Y., and Zeng, T.: East China plains: A “basin” of ozone pollution, Environ. Sci. Technol., 43(6), 1911-1915, **2009**.

Zong, R., Yang, X., Wen, L., Xu, C., Zhu, Y., Chen, T., Yao, L., Wang, L., Zhang, J., Yang, L., Wang, X., Shao, M., Zhu, T., Xue, L., and Wang, W.: Strong ozone production at a rural site in the North China Plain: Mixed effects of urban plumes and biogenic emissions, J. Environ. Sci., doi.org/10.1016/j.jes.2018.05.003, **2018**.

Supporting Information for "**Causes of a continuous summertime O_3 pollution event in Ji'nan, a central city in the North China Plain**"

Xiaopu Lyu [1], Nan Wang [2], Hai Guo [1*], Likun Xue [3], Fei Jiang [4], Yangzong Zeren [1], Hairong Cheng [5], Zhe Cai [4], Lihui Han [6] and Ying Zhou [6]

[1] Air Quality Studies, Department of Civil and Environmental Engineering, The Hong Kong Polytechnic University, Hong Kong, China

[2] Division of Environmental Meteorology, Institute of Tropical and Marine Meteorology, China Meteorology Administration, Guangzhou, China

[3] Environment Research Institute, Shandong University, Ji'nan, China

[4] Jiangsu Provincial Key Laboratory of Geographic Information Science and Technology, International Institute for Earth System Science, Nanjing University, Nanjing, China

[5] Department of Environmental Engineering, School of Resource and Environmental Sciences, Wuhan University, Wuhan, China

[6] Department of Environmental Science, College of Environmental and Energy Engineering, Beijing University of Technology, Beijing, China

Text S1 Validation of the WRF-CMAQ modeling

Due to the inevitable uncertainties inherent in chemical transport models, such as the uncertainties in emission inventory, meteorological simulation and chemical mechanisms (Hu et al., 2016), it is difficult to deduce the reasons of the discrepancies between the simulated and observed O_3 mixing ratios. However, the observations indicated extremely high levels of some VOCs on the three days when O_3 values were under-predicted. Specifically, 13.5 ppbv of ethene was observed at 14:00 LT on August 1. On August 7, 5.6 ppbv of isoprene, 16.2 ppbv of HCHO and 2.3 ppbv of hexanal were measured during 12:00 – 14:00 LT. On August 10, 22.7 ppbv of propene and 12.7 ppbv of *i*-butane were recorded at 08:00 and 16:00 LT, respectively. It is noteworthy that these mixing ratios were 5 – 10 times higher than the average mixing ratios of these VOCs. Further, most of these VOCs are highly reactive in O_3 photochemistry and may make great contributions to local O_3 production. With the setting of constant emissions of O_3 precursors, WRF-CMAQ did not reproduce these extremely high levels of VOCs, which was a plausible reason for the under-prediction of O_3 on August 1, 7 and 10. Ji'nan was behind a low pressure trough on August 9 – 10. However, vertical transport was simulated to make negative contributions to O_3 between 10:00 LT and 18:00 LT on August 10, according to the process analysis. In addition, the simulated O_3 in the upper atmosphere on August 10 was relatively low compared to that on August 5, 6 and 9 (Figure S9). Namely, the model might fail to reproduce the O_3 enhancement driven by the low pressure trough on August 10.

The process analysis indicated that horizontal and vertical transport dominated the sources of O_3 at noon (10:00-12:00 LT) and the other time periods on July 20, respectively. While vertical transport explained the high O_3 at night (Figure 2), it was not likely that horizontal transport built up O_3 at noon, because the southwesterly airflows were originated from South China and passed central China (Figure 4), where O_3 values were relatively low on that day (high O_3 occurred in Hebei province to the northwest of Ji'nan). Therefore, the overestimate of the transport effect led to the higher simulated O_3 on July 20.

Despite these discrepancies, overall the observed O_3 at the sampling site was well reproduced. In addition, the spatial distribution of the simulated O_3 was highly consistent with the observed O_3 distribution, as shown in Figure S10. The average concentrations of the simulated VOCs were also compared with the observations (Figure S11). While the day-to-day and diurnal variations of the observed VOCs were not well reproduced (not shown), which is a proverbial drawback of the WRF-CMAQ, the model reasonably simulated the magnitudes of VOCs. Moreover, the averages of the observations (Avg. Obs.) and simulations (Avg. Sim.), difference between Avg. Obs. and Avg. Sim. (Diff.), root mean square error (RMSE), normalized mean bias (NMB), normalized mean error (NME) and index of agreement (IOA) were calculated to reflect the agreements between the simulated and observed temperature (Temp.), relative humidity (R.H.), wind speed (W.S.), pressure (Press.), NO_2 and O_3, as listed in Table S4. Generally, the lower Diff., RMSE, NMB and NME, but higher IOA indicate better agreement between the simulated and observed values (Willmott et al., 1985). The validation of the simulations of air pollutants was carried out at 8 AQMSs of CNEMC in and around Ji'nan, and at the sampling site, while the meteorological parameters monitored at 6 airports in eastern and northern China and at the sampling site were used to validate the simulated meteorological conditions. The metrics calculated in this study were well within the ranges of those reported in previous studies involving WRF-CMAQ simulations (Table S4) (Jiang et al., 2010; Wang et al., 2015), suggesting good performance of the model in reproducing the meteorological conditions and air pollutants. Thus, the simulated results were accepted for further analyses.

Text S2 Source apportionment of O_3 precursors

The positive matrix factorization (PMF) model was employed to identify the sources of O_3 precursors. Details about the operation principles of PMF can be found in Paatero and Tapper (1994). Briefly, the model treats the matrix of input concentrations as the product of two matrixes (*i.e.*, factor contribution and factor profile). Here, hourly concentrations of 31 VOCs, CO, NO and NO_2 in 54 samples were input into the model. The VOCs applied for source apportionment (termed as VOCs* hereafter) were either tracers of specific sources (*e.g.*, isoprene for biogenic emissions), or having high concentrations (detectable in at least 80% samples). On average, VOCs* accounted for 79.5±11.7% of the total quantified VOCs. The uncertainties of the input concentrations of O_3 precursors were set as $\frac{5}{6} \times \mathrm{DL}$ and $\sqrt{(10\% \times concentration)^2 + (0.5 \times DL)^2}$ for the concentrations lower than and higher than DLs, respectively.

The model was run for 20 times with a random seed and the best resolution automatically given by the model was accepted. A total of 6 sources of O_3 precursors were resolved by PMF in this study. The number of sources was chosen based on the criteria that the tracers indicating different sources were not allocated in the same source, and all the sources were interpretable according to the tracers. The Bootstrap method integrated in PMF was used to estimate the uncertainties of the modelling results.

Figure S13 shows the profiles of the six sources of O_3 precursors extracted from PMF. The first source contained high levels of *n*/*i*-pentanes and aromatics, likely representing gasoline exhaust (Ho et al., 2009; Ling and Guo, 2014). The heavy hydrocarbons (C8-C10) dominated the second source, with great abundances of the combustion tracers, such as C_2-C_3 hydrocarbons, CO, NO and NO_2. These are in line with the features of diesel exhaust (Liu et al., 2008). The third source was assigned as BVOC, due to the exclusively high loading of isoprene (Guenther, 2006). The fourth source was rich in C_4 hydrocarbons, including *n*/*i*-butanes and 1,3-butadiene. It was defined as liquefied petroleum gas (LPG) usage, since butanes and butenes are present in large quantities in China's LPG (Song et al., 2008 and references therein). Solvent usage was represented by the fifth source, in view of the high loadings of hexane isomers (2,3-dimethylbutane, 2-methylpentane and 3-methylpentane) and moderate loadings of *n*-hexane, toluene, ethylbenzene and xylenes (Guo et al., 2011). At last, most of styrene, benzene, toluene, exthylbenzene and xylenes were allocated to the sixth source, which also contained moderate levels of light (C_2-C_5) hydrocarbons. Since styrene is a common petrochemical product (Jobson et al., 2004; Liu et al., 2008), this source was designated as petrochemical industry.

The source contributions to the O_3 production rates were obtained from the differences in simulated O_3 production rates between a base run and a constrained run. In the base run, the O_3 production rate was simulated with the observed concentrations of air pollutants except for the carbonyls, while the concentrations of air pollutants attributable to a specific source were deducted from the observed concentrations for the input of the constrained run. To account for the influence of primary hydrocarbons on the formation of carbonyls, and the subsequent impact on O_3 production, carbonyls were not constrained to observations in either the base run or the constrained runs. However, the source-specific primary emissions of carbonyls and their contributions to O_3 production were not considered in this approach. Therefore, the source-specific contributions to net O_3 production rates were expected to be underestimated, as carbonyls are generally of high O_3 formation potentials (Cheng et al., 2010; Dong et al., 2014). The method was applied to each of the six sources, derived from the PMF analysis, thereby acquiring the contribution to O_3 production rates of each source.

Text S3 Definitions of the O_3 formation regimes

As shown in Figure 8, O_3 formation was divided into $VOC^{\#}$-limited regime and NO_x-limited regime with the method used in Lyu et al. (2017). Briefly, at a given $OH\ reactivity_{VOCs^{\#}}$ value, the simulated O_3 production rate generally got the maximum at a specific $OH\ reactivity_{NOx}$ value due to the dual role of NO_x in O_3 formation. This specific $OH\ reactivity_{NOx}$ value was treated as the dividing point between NO_x-limited regime and $VOC^{\#}$-limited regime at the given $OH\ reactivity_{VOCs^{\#}}$ value. Since the scenarios involved 14 gradients of $OH\ reactivity_{VOCs^{\#}}$ (10% - 140% with the step of 10%), 14 pairs of $OH\ reactivity_{NOx}$ and $OH\ reactivity_{VOCs^{\#}}$ were obtained, as shown in the orange crosses in Figure 8. A dividing line was acquired from the linear regression between $OH\ reactivity_{VOCs^{\#}}$ and $OH\ reactivity_{NOx}$ in these scenarios (presented in orange dashed line in Figure 8). O_3 formation was limited by $VOCs^{\#}$ and NO_x in the lower right and upper left areas of the dividing line, respectively. Since the horizontal and vertical coordinates were the percentages relative to the average $OH\ reactivity_{VOCs^{\#}}$ and $OH\ reactivity_{NOx}$ during O_3 episodes, rather than the actual values of OH reactivity, we did not calculate the dividing ratio of $\frac{OH\ reactivity_{VOCs^{\#}}}{OH\ reactivity_{NOx}}$ here. Further, it was found that the O_3 production rates were also enhanced with the increase of

$OH\ reactivity_{VOCs^{\#}}$ in the upper left area close to the dividing line. We defined it as a transitional regime where the O_3 formation was comparably sensitive to VOCs$^{\#}$ and NO_x. Beyond the transitional regime in the upper left area of the dividing line, the sensitivity of O_3 formation to NO_x was generally ten times higher than to VOCs$^{\#}$, which was designated as NO_x-limited regime. The transitional regime and the NO_x-limited regime were divided by the blue dashed line in Figure 8.

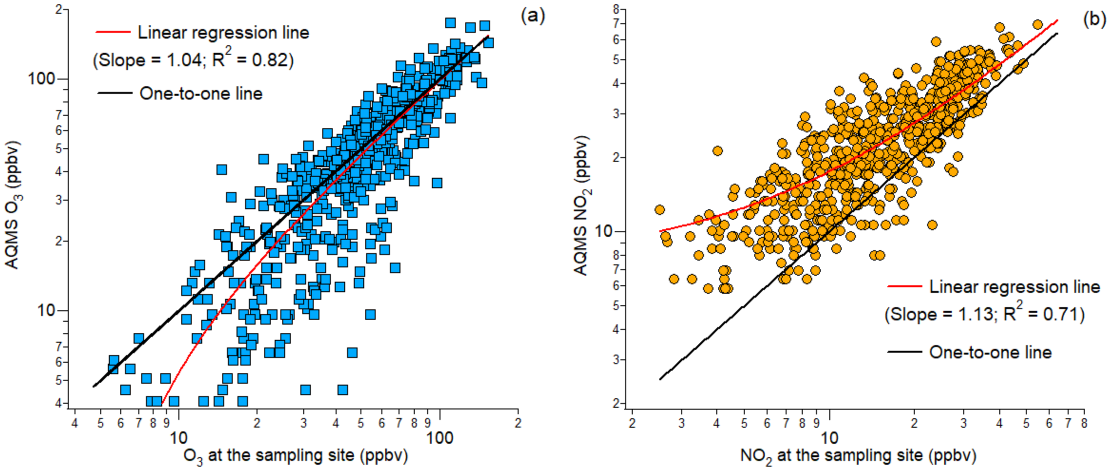

Figure S1. Agreement of the hourly (a) O_3 and (b) NO_2 between our observations on the campus of Shandong University and those monitored at the nearest AQMS by CNEMC.

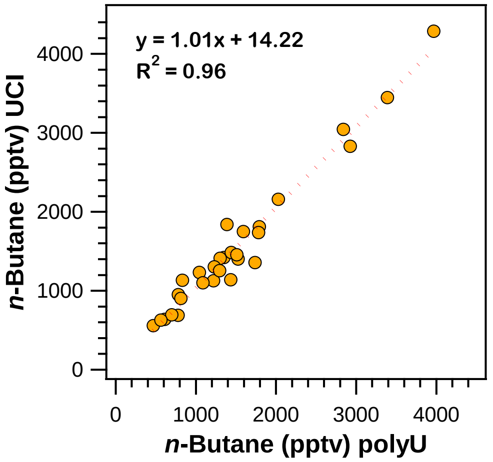

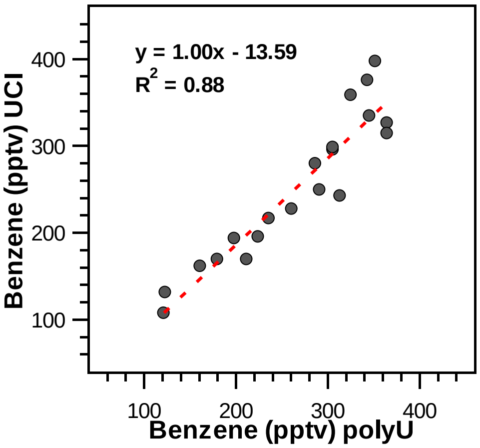

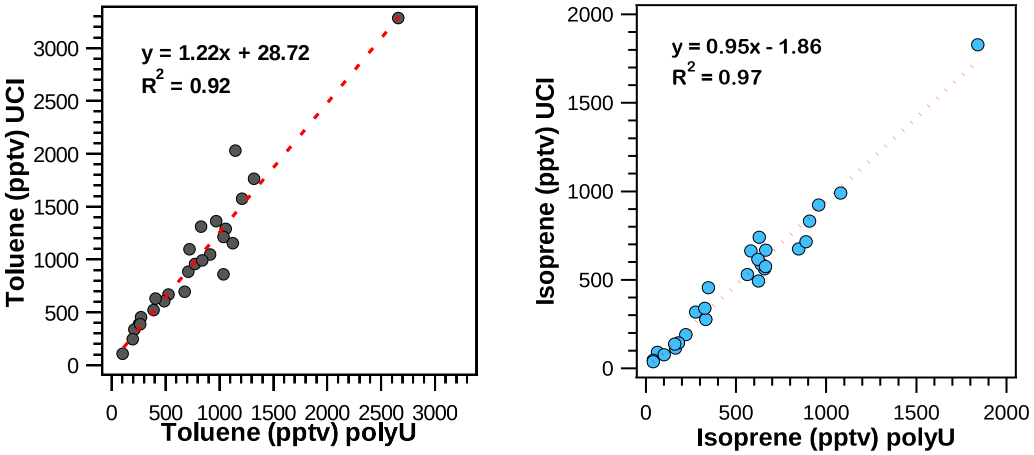

Figure S2. Inter-comparison of VOC analysis results between our laboratory (x axis) and Prof. Donald Blake's group (y axis). *n*-butane, benzene, toluene and isoprene are selected as examples. The red dashed line represents the linear regression between VOCs analyzed in two laboratories.

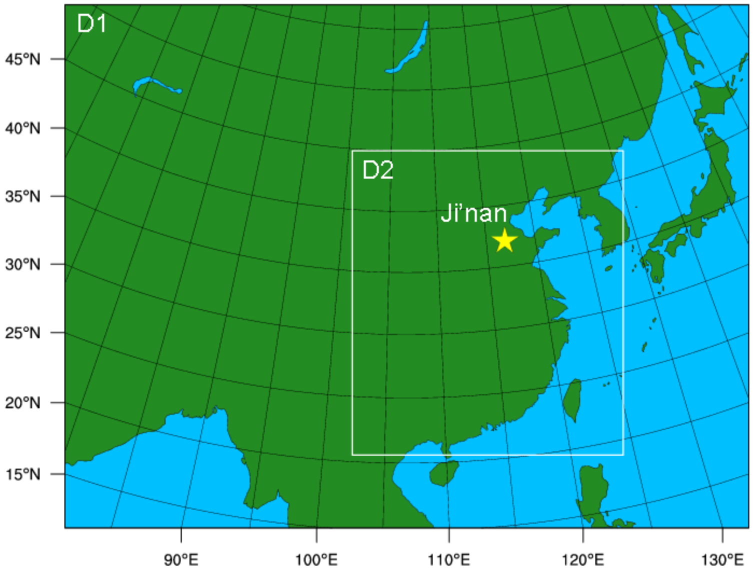

Figure S3. Settings of the two-nested domains for the WRF-CMAQ model. D1 and D2 are the outer and inner domains, covering the entire continental area of China and eastern China, respectively. The yellow star represents Ji'nan.

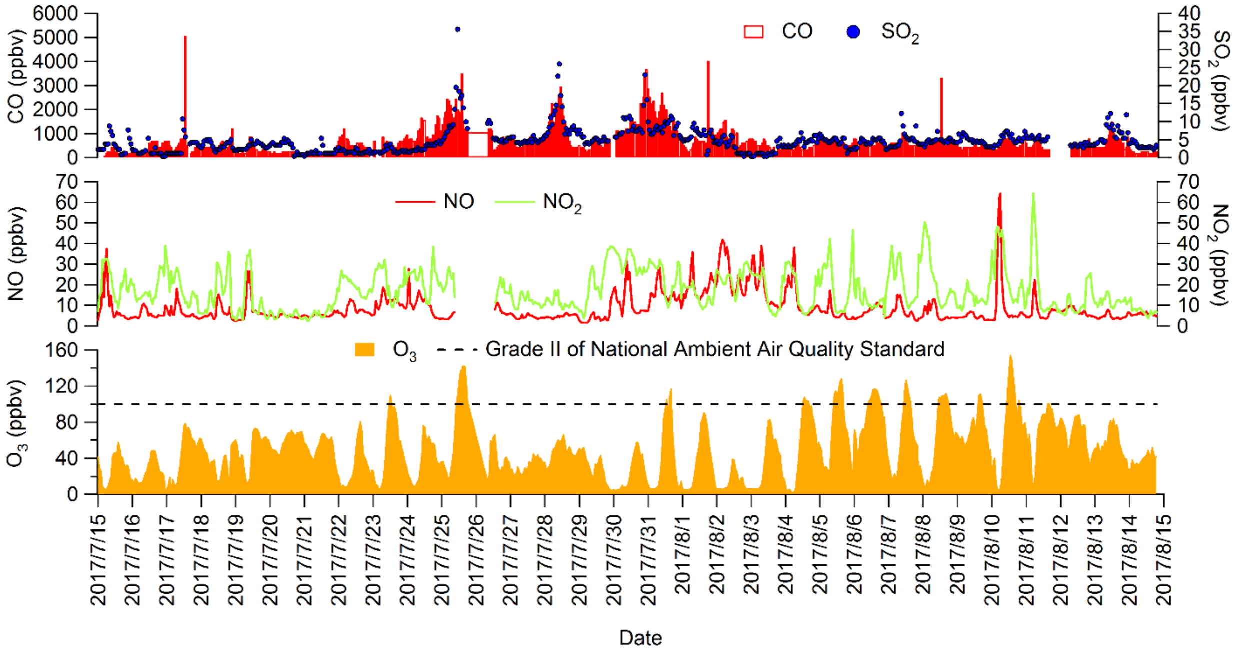

Figure S4. Hourly variations of trace gases monitored at the sampling site (O_3, NO and NO_2) and at the nearest AQMS (CO and SO_2) during July 15-August 14, 2017.

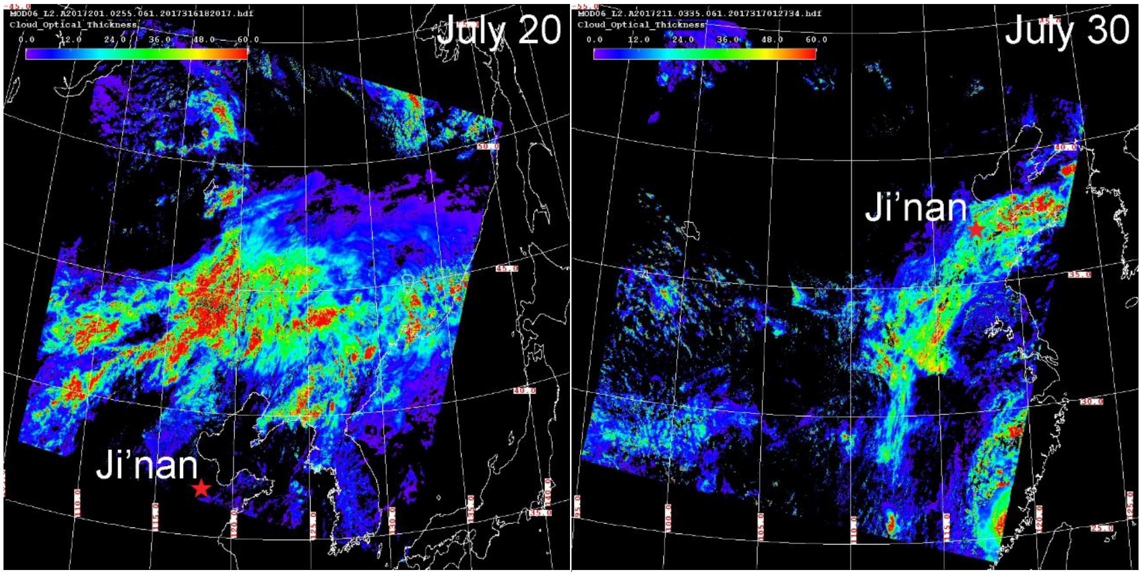

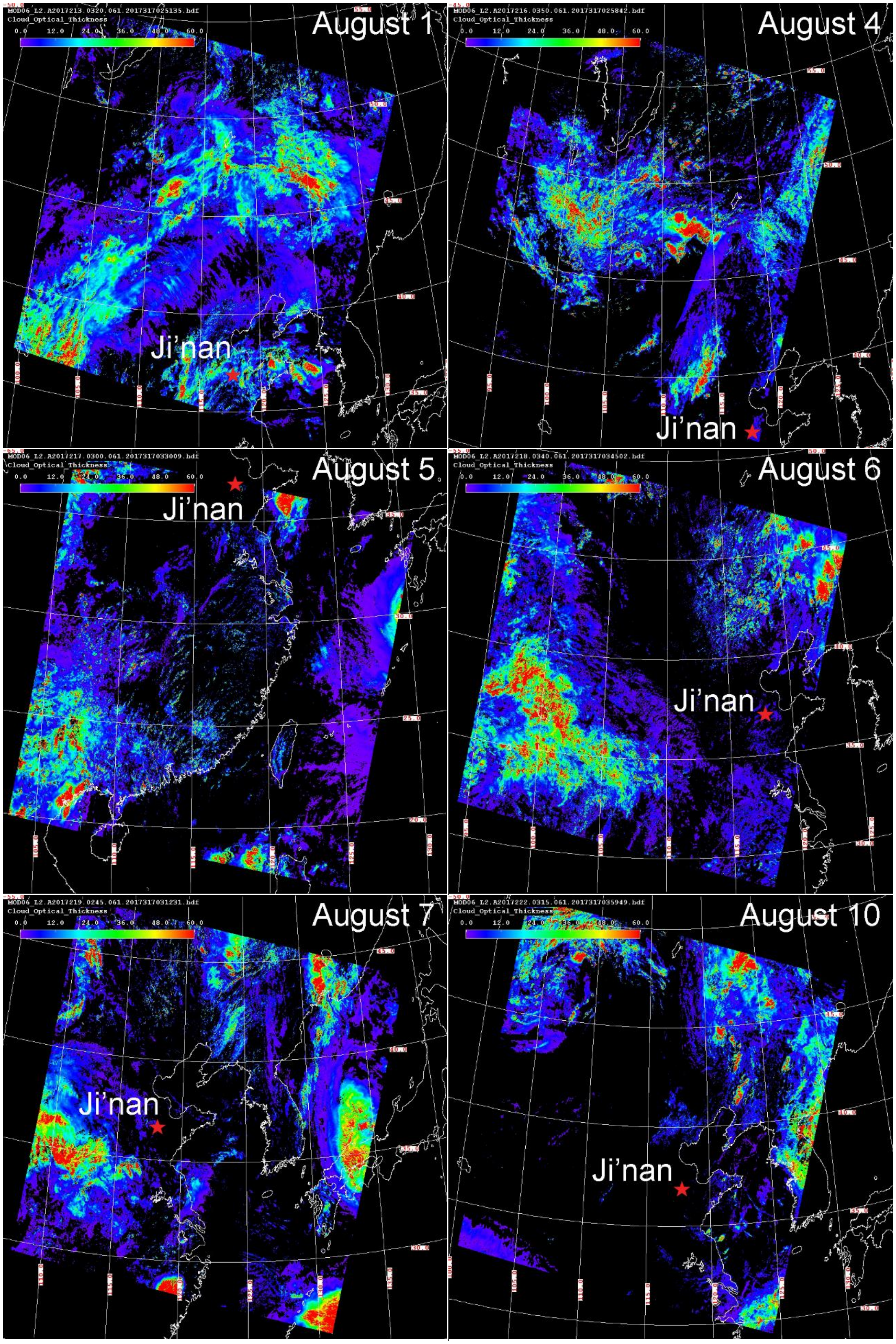
MOD06_L2.A2017213.0320.061.2017317025135.hdf
Cloud_Optical_Thickness
0.0 12.0 24.0 36.0 48.0 60.0
August 1
Ji'nan
MOD06_L2.A2017216.0350.061.2017317025842.hdf
Cloud_Optical_Thickness
0.0 12.0 24.0 36.0 48.0 60.0
August 4
Ji'nan
MOD06_L2.A2017217.0300.061.2017317033009.hdf
Cloud_Optical_Thickness
0.0 12.0 24.0 36.0 48.0 60.0
August 5
Ji'nan
MOD06_L2.A2017218.0340.061.2017317034502.hdf
Cloud_Optical_Thickness
0.0 12.0 24.0 36.0 48.0 60.0
August 6
Ji'nan
MOD06_L2.A2017219.0245.061.2017317031231.hdf
Cloud_Optical_Thickness
0.0 12.0 24.0 36.0 48.0 60.0
August 7
Ji'nan
MOD06_L2.A2017222.0315.061.2017317035949.hdf
Cloud_Optical_Thickness
0.0 12.0 24.0 36.0 48.0 60.0
August 10
Ji'nan

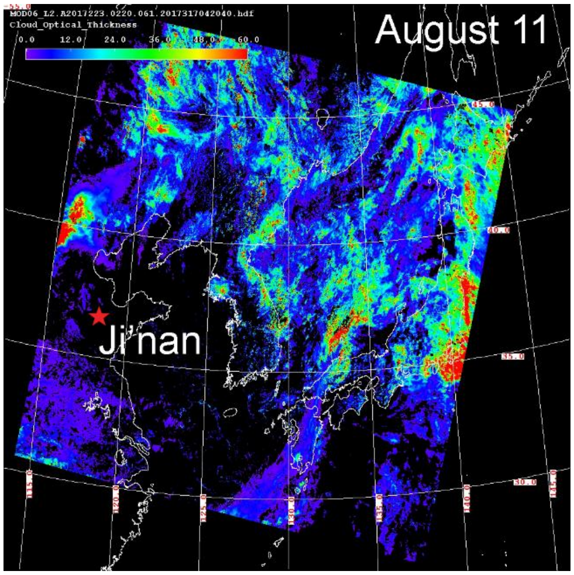

Figure S5. Cloud optical depth (COD) retrieved from terra/MODIS at noon (10:30 – 12:00 LT) of the canister sampling days. The color scale denotes for the COD within the range of 0 (purple) to 60 (red). The red star denotes Ji'nan.

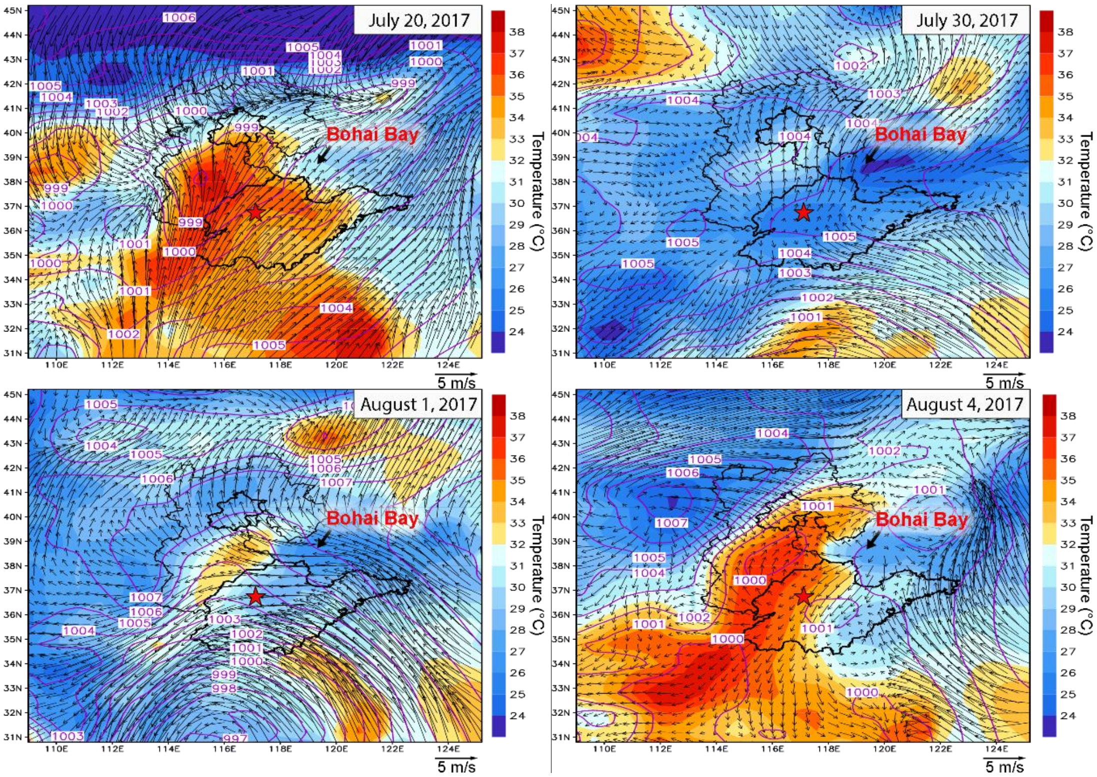

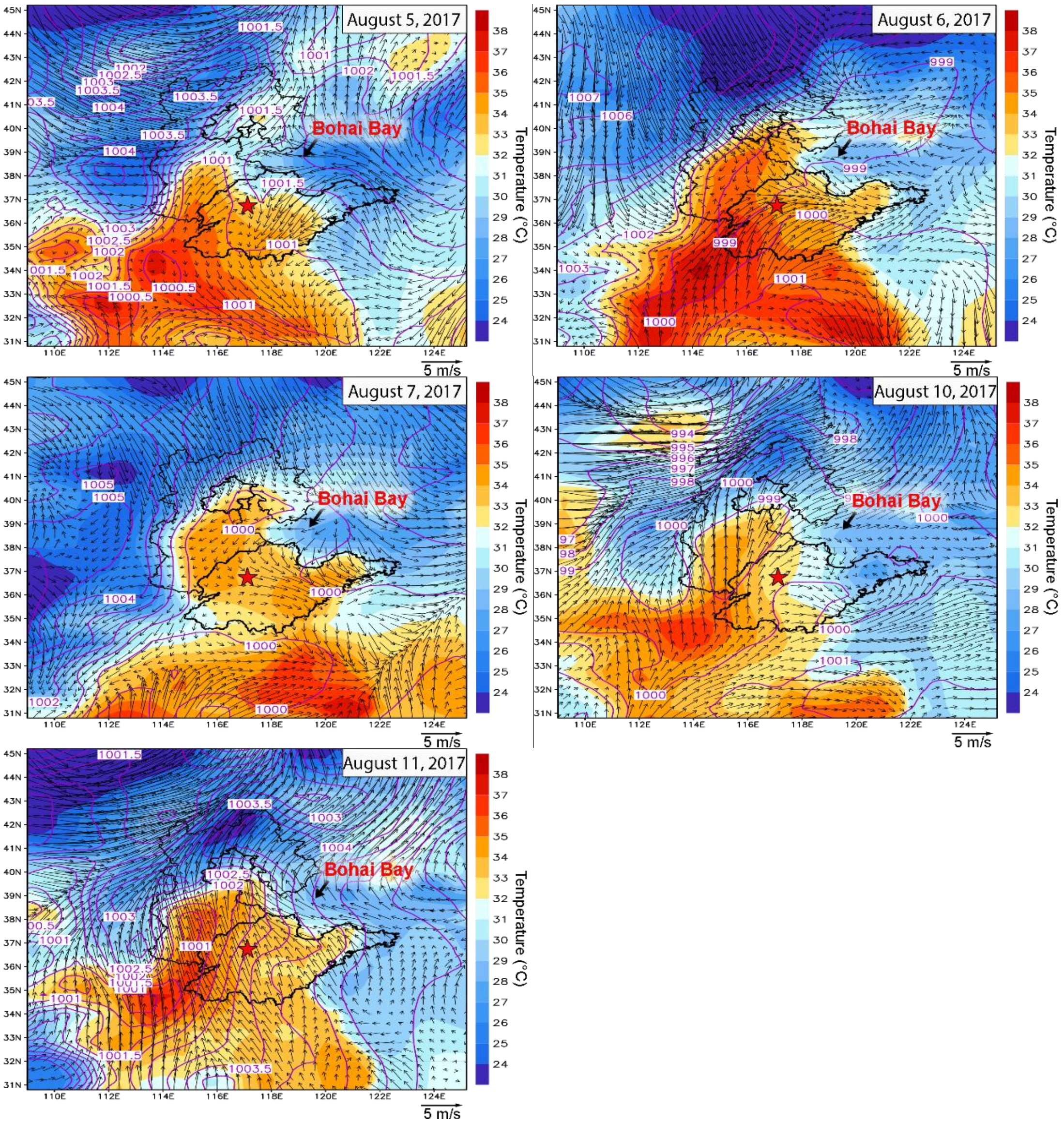

Figure S6. Weather charts at 14:00 LT on individual VOC sampling days. The red star denotes for Ji'nan. The dark black line is the boundary of Shandong province. Bohai Bay is located to the northeast of Shandong province. Numbers in the figure are sea-level pressures in unit of hPa.

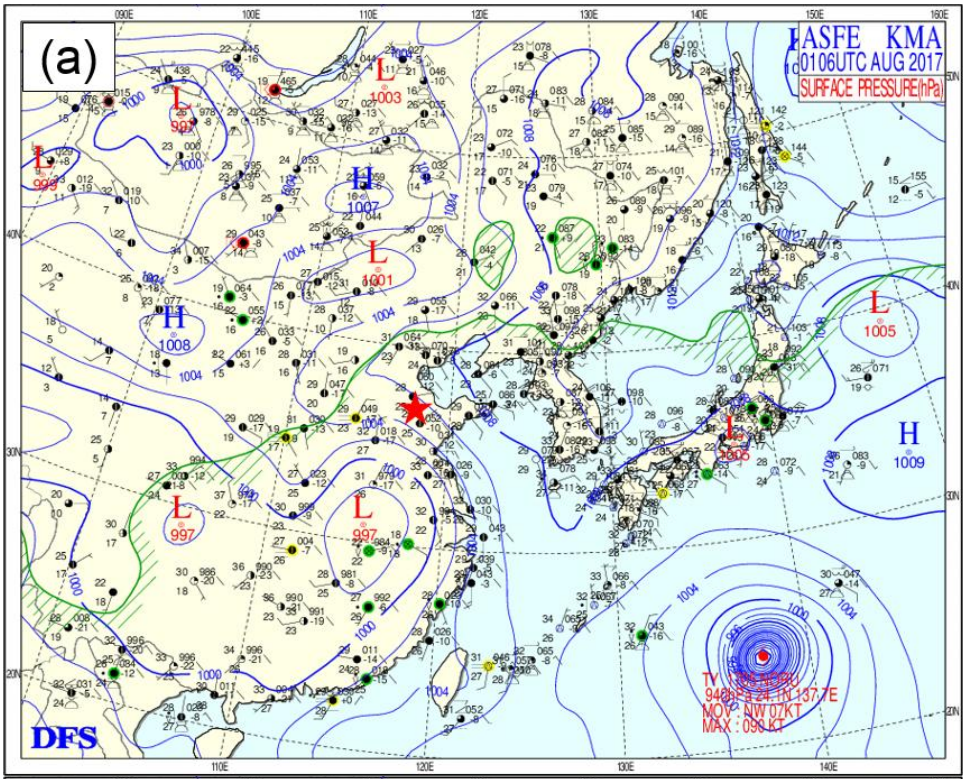
(a)
ASFE KMA
0106UTC AUG 2017
SURFACE PRESSURE(hPa)
DFS
TY 1705 NORU
940hPa 24.1N 137.7E
MOV : NW 07KT
MAX : 090 KT
H
1008
H
1007
H
1009
L
1003
L
1001
L
997
L
997
L
1005
L
1005
1000
1004
1008
090E
100E
110E
120E
130E
140E
150E
160E
20N
30N
40N
50N

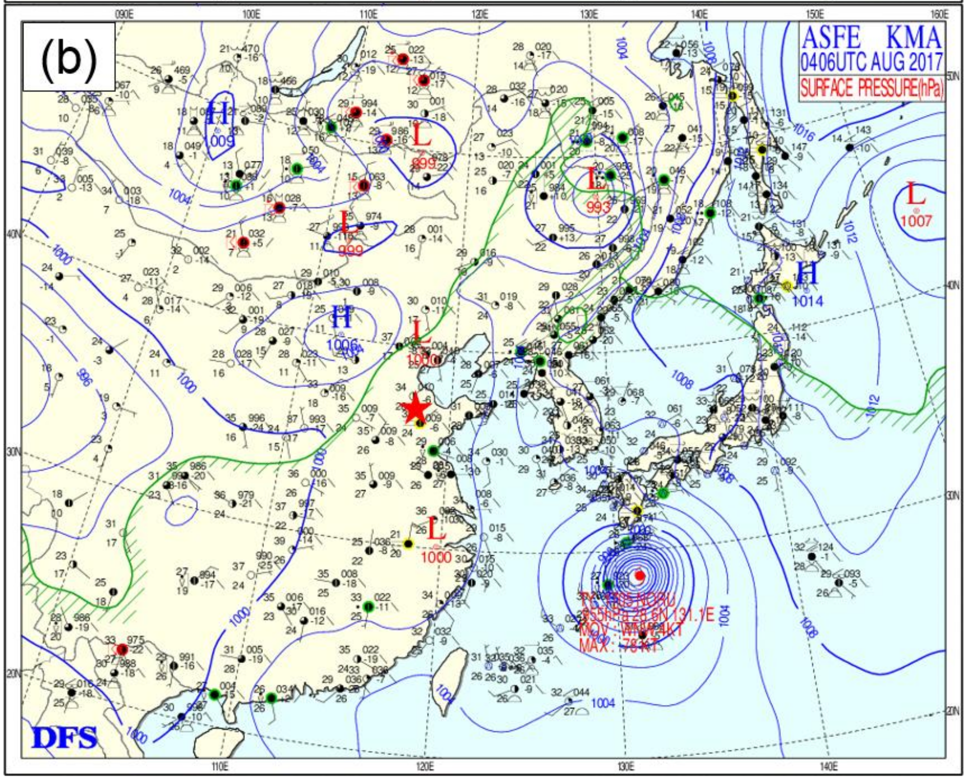
(b)
ASFE KMA
0406UTC AUG 2017
SURFACE PRESSURE(hPa)
DFS
TY 1705 NORU
955hPa 28.6N 131.1E
MOV : WNW 04KT
MAX : 75 KT
H
1009
H
1006
H
1014
L
999
L
999
L
993
L
1000
L
1000
L
1007
996
1000
1004
1008
1012
1016
090E
100E
110E
120E
130E
140E
150E
160E
20N
30N
40N
50N

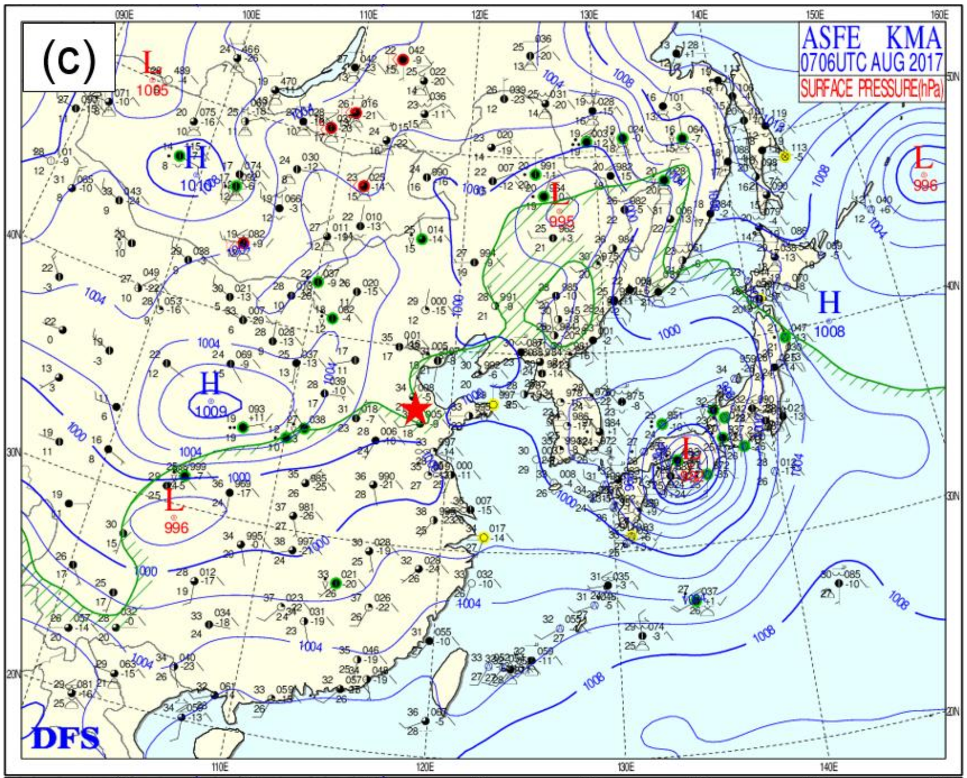
(c)
ASFE KMA
0706UTC AUG 2017
SURFACE PRESSURE(hPa)
DFS

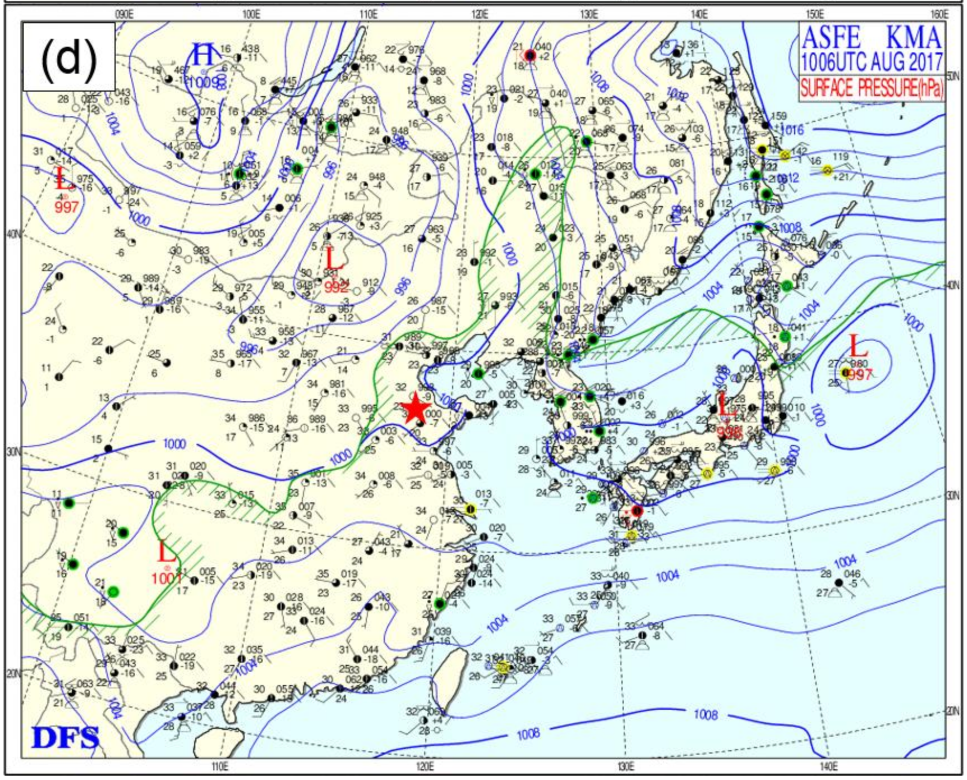
(d)
ASFE KMA
1006UTC AUG 2017
SURFACE PRESSURE(hPa)
DFS

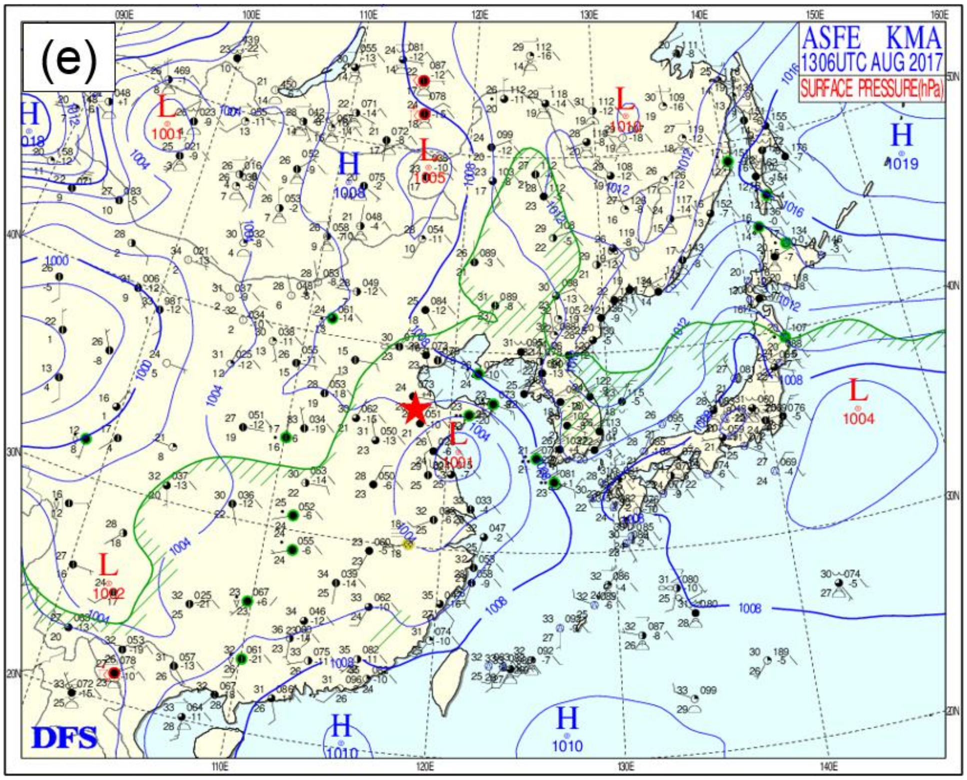

Figure S7. Weather chart over the Northeast Asia on (a) August 01, (b) August 04, (c) August 07, (d) August 10 and (e) August 13 at 06:00 UTC (14:00 LT) at surface level. The red star denotes Ji'nan city. The capital letters "H" and "L" represent high pressure center and low pressure center, respectively. Blue lines are the sea level isobars. Green line is the isometric humidity line with the specific humidity of ≥15g/kg on the grid side. All the charts can be accessed through the link: http://222.195.136.24/forecast.html.

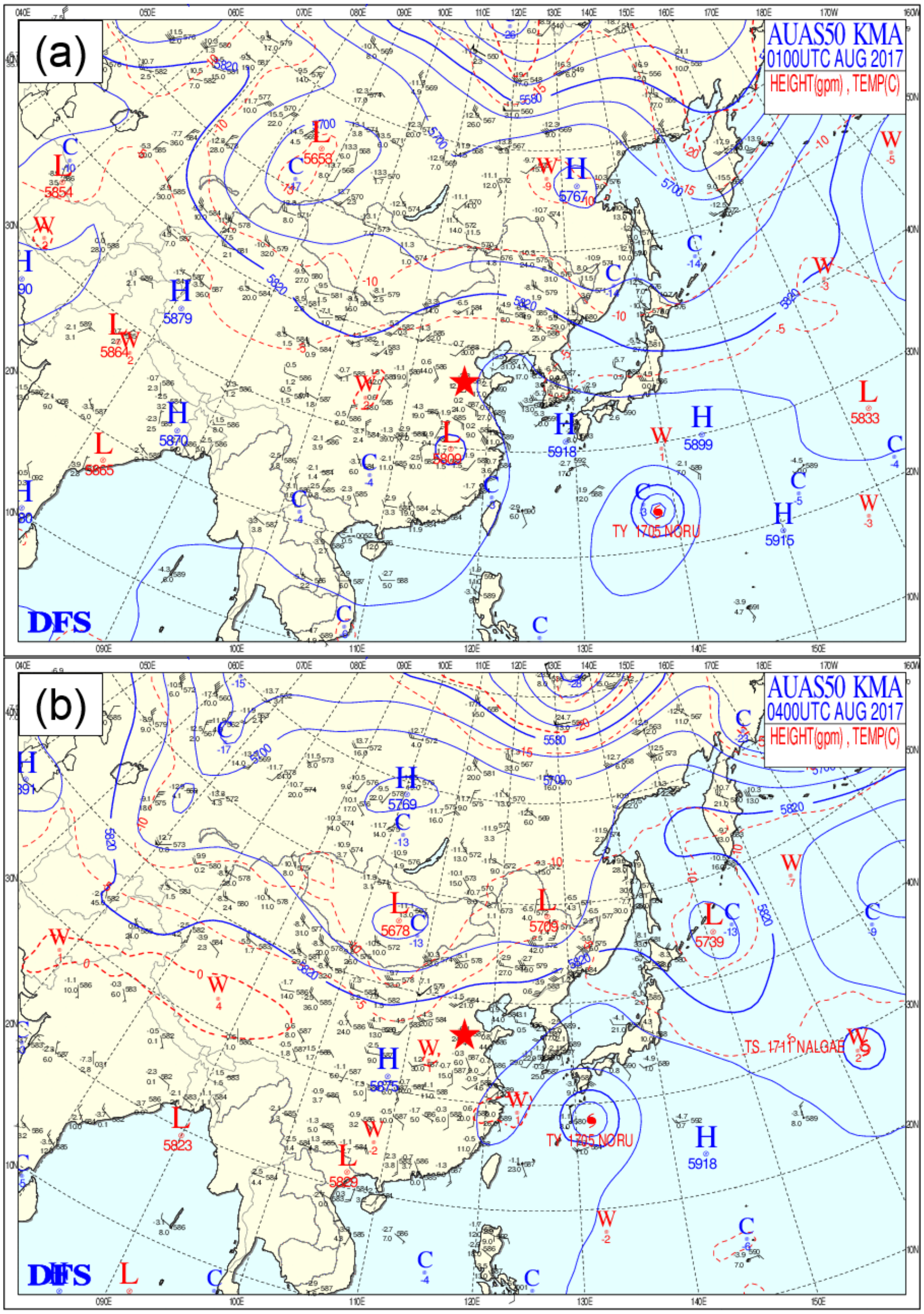
(a)
AUAS50 KMA
0100UTC AUG 2017
HEIGHT(gpm) , TEMP(C)
TY 1705 NORU
DFS
(b)
AUAS50 KMA
0400UTC AUG 2017
HEIGHT(gpm) , TEMP(C)
TY 1705 NORU
TS 1711 NALGAE
DFS

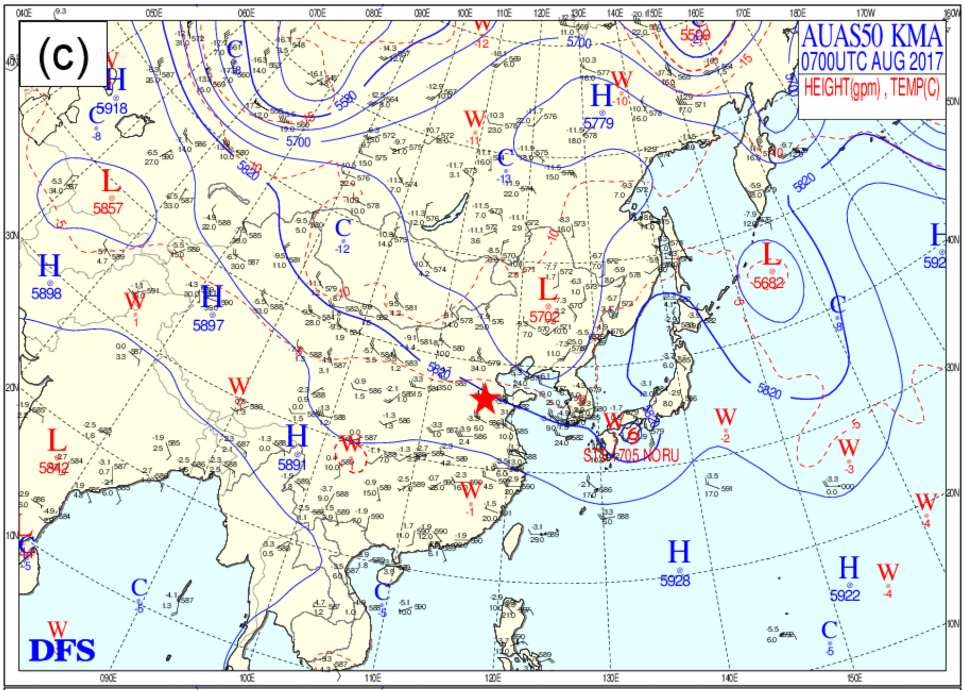
(c)
AUAS50 KMA
0700UTC AUG 2017
HEIGHT(gpm) , TEMP(C)
DFS
STS 1705 NORU
5700
5820
5880

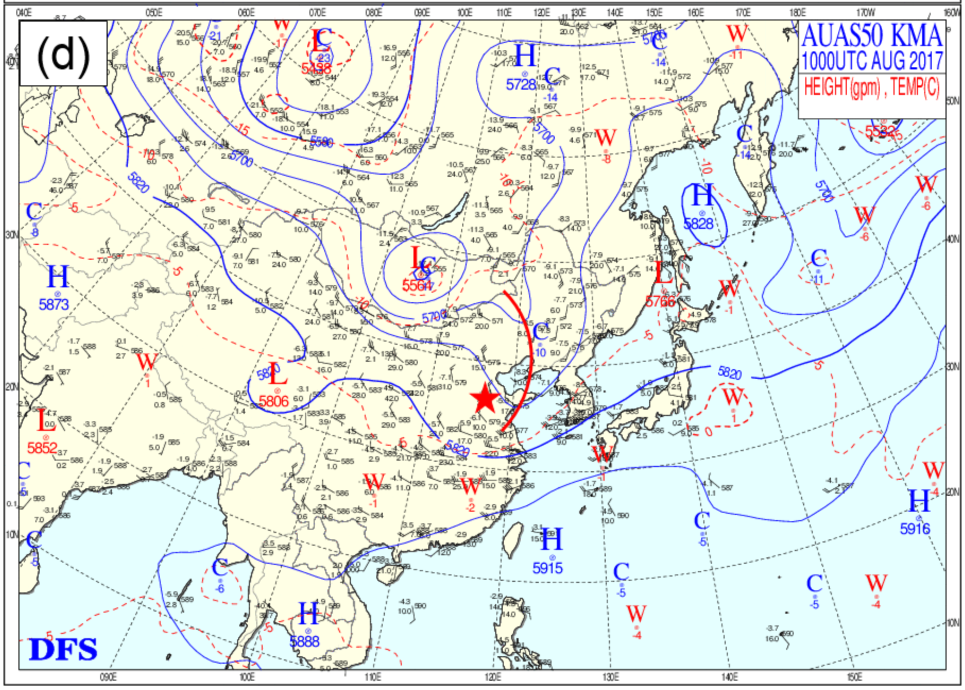
(d)
AUAS50 KMA
1000UTC AUG 2017
HEIGHT(gpm) , TEMP(C)
DFS
5700
5820
5880

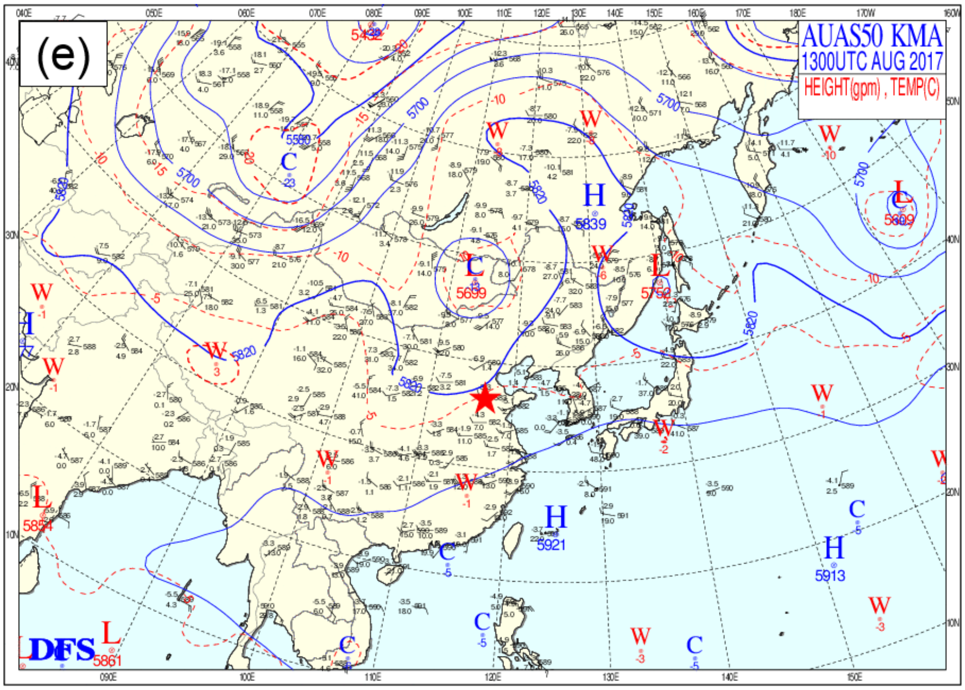

Figure S8. Weather chart over the Northeast Asia on (a) August 01, (b) August 04, (c) August 07, (d) August 10 and (e) August 13 at 00:00 UTC (08:00 LT) at altitude of 500 hPa. The red star denotes Ji'nan city. The capital letters "H" and "L" represent high pressure center and low pressure center, respectively. Blue lines are the 500 hPa geopotential height (gpm) lines. The red curve in panel (d) demonstrates the low pressure trough. All the charts can be accessed through the link: http://222.195.136.24/forecast.html.

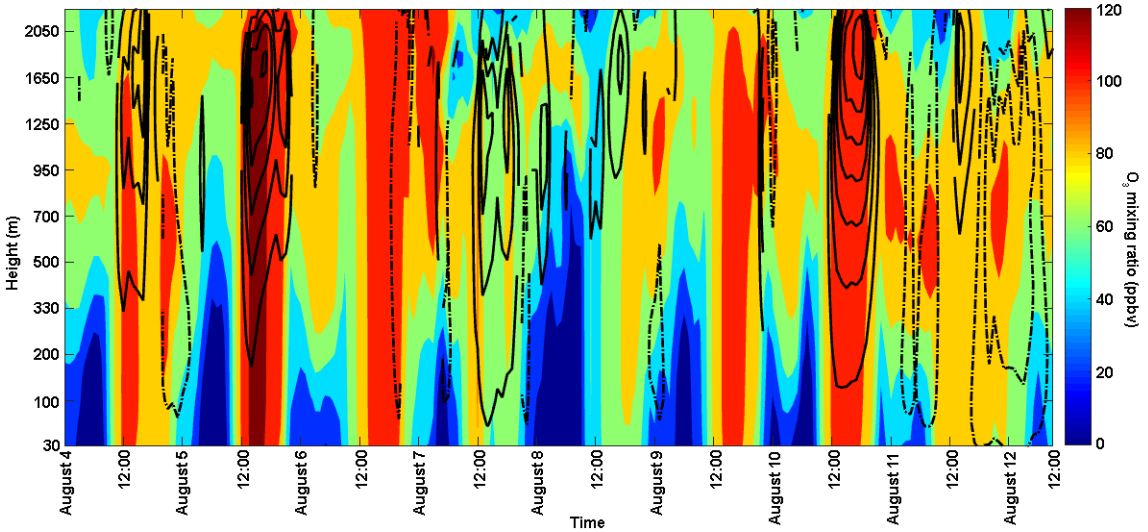

Figure S9. Vertical profile of the simulated O_3 over Ji'nan during August 4-11. The black solid and dotted lines represent the updraft and downdraft simulated by WRF-CMAQ, respectively. The areas with no line indicate that there were no simulated winds in vertical direction.

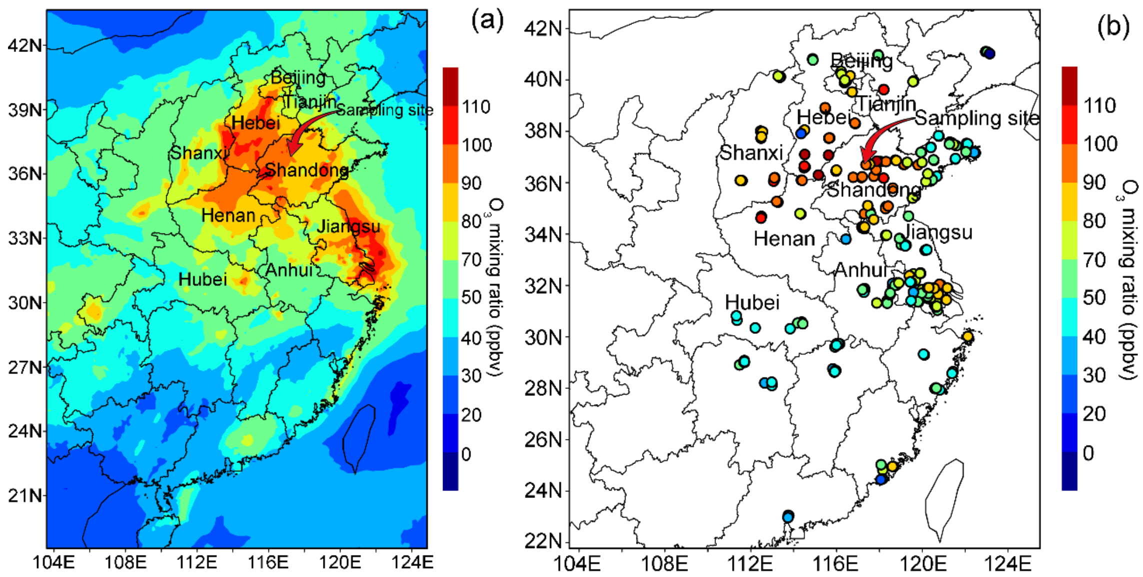

Figure S10. Comparison between the spatial distributions of (a) the WRF-CMAQ simulated O_3 and (b) the observed O_3 at 14:00 LT averaged over August 4-11. The observed O_3 is acquired from the AQMSs of CNEMC.

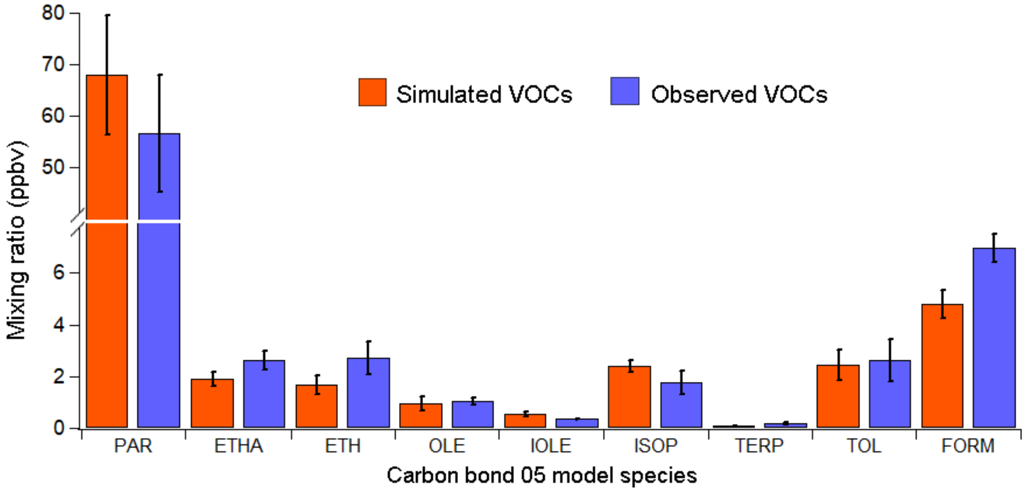

Figure S11. Comparison between the averages of the hourly observed and WRF-CMAQ simulated VOCs. PAR: paraffin carbon bond; ETHA: ethane; ETH: ethene; OLE: terminal olefin carbon bond; IOLE: internal olefin carbon bond; ISOP: isoprene; TERP: terpene; TOL: toluene and other monoalkyl aromatics; FORM: formaldehyde. The matrix of assignments from real compounds to carbon bond 05 model species can be found in Yarwood et al. (2005).

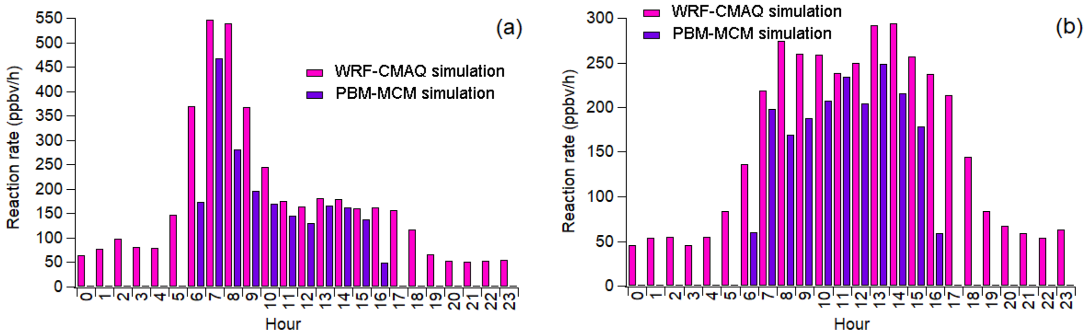

Figure S12. Average diurnal cycle of "NO+O_3" reaction rates simulated by WRF-CMAQ and PBM-MCM during (a) O_3 episodes and (b) non-episodes.

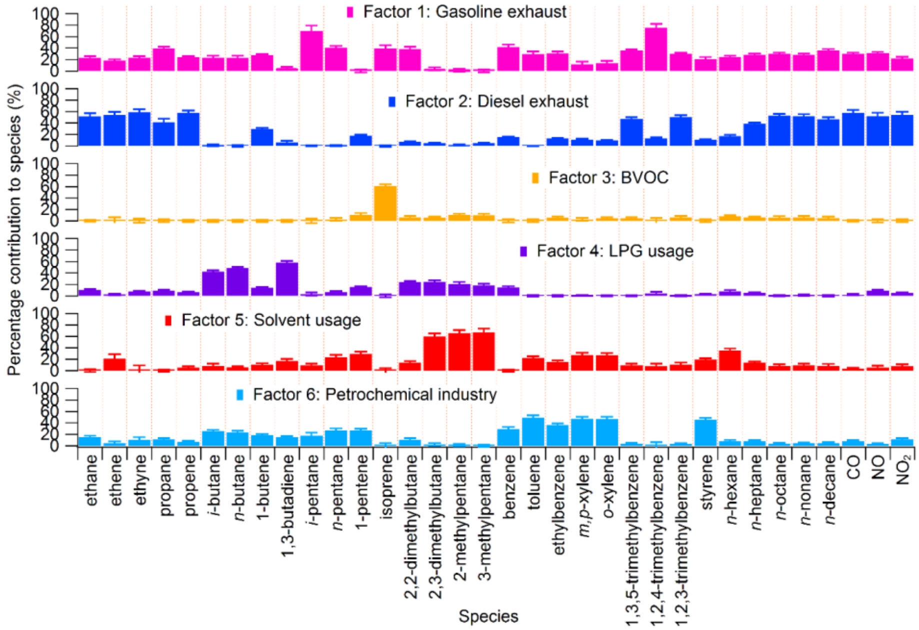

Figure S13. Profiles of the six sources of O_3 precursors identified for the samples collected in daytime of the VOC sampling days in Ji'nan.

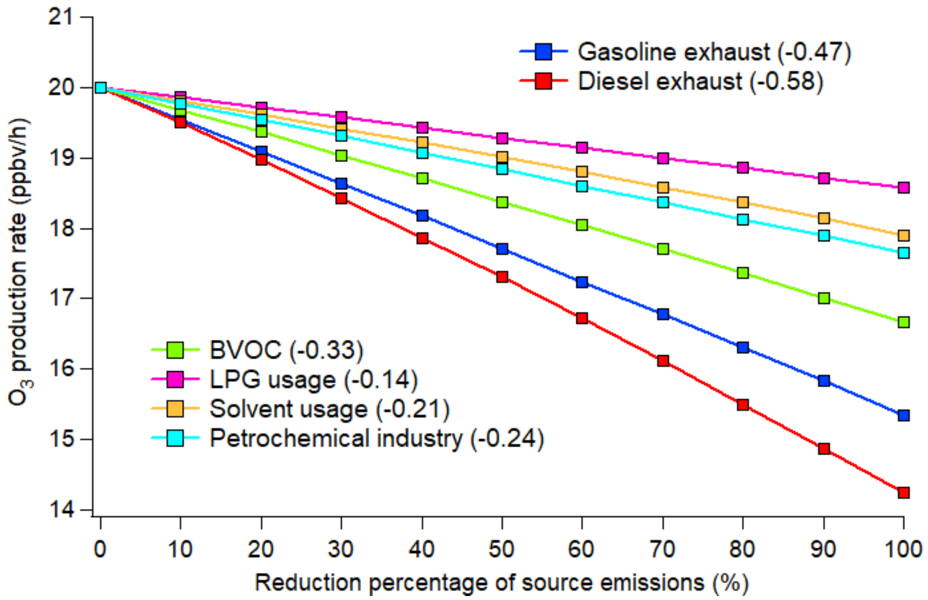

Figure S14. Average O_3 production rate at 12:00 LT during O_3 episodes as a response of the reduction percentages of source emissions. Numbers in the brackets are the average O_3 reduction efficiencies (ppbv/10% reduction in source emissions).

Species	Site	Instrument	Resolution	Accuracy	Precision	Detection limit
SO_2	AQMS*	API, Model 100 E	20 sec	<20%	0.5% of reading above 50 ppbv	0.4 ppbv
CO	AQMS	API, Model 300 E	10 sec	<20%	0.5% of reading	40 ppbv
NO-NO_2-NO_x	AQMS	API, model 200E	20 sec	<20%	0.5% of reading	0.4 ppbv
	Campus site #	Thermo, Model 42C	1 min	<15%	0.4 ppbv	0.4 ppbv
O_3	AQMS	API, model 400E	10 sec	<20%	<0.5% of reading	0.6 ppbv
	Campus site	Thermo, Model 49C	20 sec	<15%	1.0 ppbv	1.0 ppbv

* An air quality monitoring station of China National Environmental Monitoring Center closest to our sampling site in the campus of Shandong University; # Our sampling site on the campus of Shandong University.

Table S1. Descriptions of the trace gas analyzers used in this study.

Date	Episode/Non-episode	$J(O^1D)$ (s^{-1})	JNO_2 (s^{-1})
July 20	Non-episode	3.40×10^{-5}	9.27×10^{-3}
July 30	Non-episode	1.02×10^{-5}	2.73×10^{-3}

August 1	Non-episode	2.71×10^{-5}	7.50×10^{-3}
August 4	Episode	2.85×10^{-5}	7.95×10^{-3}
August 5	Episode	2.69×10^{-5}	7.50×10^{-3}
August 6	Episode	2.75×10^{-5}	7.70×10^{-3}
August 7	Episode	2.34×10^{-5}	6.52×10^{-3}
August 10	Episode	3.07×10^{-5}	8.72×10^{-3}
August 11	Episode	2.90×10^{-5}	8.25×10^{-3}

Table S2. Daily maximum photolysis rates of O_3 and NO_2 on VOC sampling days in Ji'nan.

OH reactivity of species X	Full name of species/VOC groups	Species included
RNO	Nitric oxide	Nitric oxide
RNO2	Nitrogen dioxide	Nitrogen dioxide
RCO	Carbon monoxide	Carbon monoxide
RCarbonyls	Carbonyls	Formaldehyde, acetaldehyde, acetone, hexanal
RBVOCs	Biogenic VOCs	Isoprene, *α*-pinene, *β*-pinene
RAromatics	Aromatics	Benzene, toluene, ethylbenzene, *m*/*p*-xylenes, *o*-xylene
RAlkenes	Alkenes	Ethene, ethyne, propene, 1-/*i*-butene, 1,3-butadiene, *trans*-2-butene, *cis*-2-butene, 1-pentene
RAlkanes	Alkanes	Ethane, propane, *n*/*i*-butanes, *n*/*i*-pentanes

Table S3. Full name of inorganic trace gases and VOC species for the calculation of OH reactivity.

Meteorological parameter/Air pollutant	Avg. Obs.	Avg. Sim.	Diff.	RMSE	NMB	NME	IOA
Temp. (°C)	30.0	30.7	0.7	2.4	0.02	0.06	0.89
R.H. (%)	72.7	67.5	-5.2	14.4	-0.06	0.15	0.82
W.S. (m/s)	2.8	3.3	0.5	1.5	0.38	0.56	0.74
Press. (hPa)	1000.5	998.8	-1.7	4.0	-0.002	0.003	0.56
NO_2 (ppbv)	26.7	28.4	1.7	16.7	0.18	0.58	0.73
O_3 (ppbv)	62.8	52.4	-10.4	24.0	-0.07	0.48	0.89

Table S4. Statistical comparisons of the WRF-CMAQ simulated and observed meteorological parameters, O_3 and NO_2. The comparisons are made for the hourly data in 24 hours on all the VOC sampling days.

O_3 production pathway	O_3 destruction pathway
$HO_2 + NO$	$OH + NO_2$
$RO_2 + NO$	$O^1(D) + H_2O$
	$O_3 + OH$
	$O_3 + HO_2$
	O_3 + alkenes

Table S5. Production and destruction pathways of O_3.

References:

Dong, D., Shao, M., Li, Y., Lu, S., Wang, Y., Ji, Z., and Tang, D.: Carbonyl emissions from heavy-duty diesel vehicle exhaust in China and the contribution to ozone formation potential, J. Environ. Sci., 26(1), 122-128, **2014**.

Guenther, A., Karl, T., Harley, P., Wiedinmyer, C., Palmer, P.I., and Geron, C.: Estimates of global terrestrial isoprene emissions using MEGAN (Model of Emissions of Gases and Aerosols from Nature), Atmos. Chem. Phys., 6(11), 3181-3210, **2006**.

Guo, H., Cheng, H.R., Ling, Z.H., Louie, P.K., and Ayoko, G.A.: Which emission sources are responsible for the volatile organic compounds in the atmosphere of Pearl River Delta?, J. Hazard. Mat., 188(1-3), 116-124, **2011**.

Ho, K.F., Lee, S.C., Ho, W.K., Blake, D.R., Cheng, Y., Li, Y.S., Ho, S.S., Fung, K., Louie, P.K., and Park, D.: Vehicular emission of volatile organic compounds (VOCs) from a tunnel study in Hong Kong, Atmos. Chem. Phys., 9(19), 7491-7504, **2009**.

Hu, J., Chen, J., Ying, Q., and Zhang, H.: One-year simulation of ozone and particulate matter in China using WRF/CMAQ modeling system, Atmos. Chem. Phys., 16(16), 10333–10350, **2016**.

Jiang, F., Guo, H., Wang, T.J., Cheng, H.R., Wang, X.M., Simpson, I.J., Ding, A.J., Saunders, S.M., Lam, S.H.M., and Blake, D.R.: An ozone episode in the Pearl River Delta: Field observation and model simulation, J. Geophys. Res. – Atmos., 115(D22), **2010**.

Jobson, B.T., Berkowitz, C.M., Kuster, W.C., Goldan, P.D., Williams, E.J., Fesenfeld, F.C., Apel, E.C., Karl, T., Lonneman, W.A., and Riemer, D.: Hydrocarbon source signatures in Houston, Texas: Influence of the petrochemical industry, J. Geophys. Res. – Atmos., 109(D24), doi.org/10.1029/2004JD004887, **2004**.

Ling, Z.H. and Guo, H.: Contribution of VOC sources to photochemical ozone formation and its control policy implication in Hong Kong, Environ. Sci. Policy, 38, 180-191, **2014**.

Liu, Y., Shao, M., Fu, L., Lu, S., Zeng, L., and Tang, D.: Source profiles of volatile organic compounds (VOCs) measured in China: Part I, Atmos. Environ., 42(25), 6247-6260, **2008**.

Lyu, X.P., Guo, H., Wang, N., Simpson, I.J., Cheng, H.R., Zeng, L.W., Saunders, S.M., Lam, S. H.M., Meinardi, S., and Blake, D.R.: Modeling C1-C4 alkyl nitrate photochemistry and their impacts on O3 production in urban and suburban environments of Hong Kong, J. Geophys. Res. – Atmos., 122(19), **2017**.

Paatero, P. and Tapper, U.: Positive matrix factorization: A non-negative factor model with optimal utilization of error estimates of data values, Environmetrics, 5(2), 111-126, **1994**.

Song, Y., Dai, W., Shao, M., Liu, Y., Lu, S., Kuster, W., and Goldan, P.: Comparison of receptor models for source apportionment of volatile organic compounds in Beijing, China, Environ. Pollut., 156(1), 174-183, **2008**.

Wang, N., Guo, H., Jiang, F., Ling, Z.H., and Wang, T.: Simulation of ozone formation at different elevations in mountainous area of Hong Kong using WRF-CMAQ model, Sci. Total Environ., 505, 939-951, **2015**.

Willmott, C.J., Ackleson, S.G., Davis, R.E., Feddema, J.J., Klink, K.M., Legates, D.R., O'Donnell, J., and Rowe, C.M.: Statistics for the evaluation and comparison of models, J. Geophys. Res. - Oceans, 90(C5), 8995-9005, **1985**.